

UNIVERSITÀ DEGLI STUDI DI TRIESTE

FACOLTÀ DI SCIENZE MATEMATICHE, FISICHE E NATURALI

CORSO DI LAUREA SPECIALISTICA IN FISICA

INTERPLAY BETWEEN THE DRUDE ELECTRONS LIFETIME AND PLASMA FREQUENCY IN THE NON-EQUILIBRIUM OPTICAL PROPERTIES OF HIGH-TEMPERATURE SUPERCONDUCTORS

Laureando:

Tadesse Abebaw

Matricola N. 62300165

Relatore:

Prof. Fulvio Parmigiani

Correlatore:

Dott. Giacomo Coslovich

ANNO ACCADEMICO 2009/10

© 2010 by Tadesse
All rights reserved

ABSTRACT

INTERPLAY BETWEEN THE DRUDE ELECTRONS LIFETIME AND PLASMA FREQUENCY IN THE NON-EQUILIBRIUM OPTICAL PROPERTIES OF HIGH-TEMPERATURE SUPERCONDUCTORS.

October 2010

Time-resolved optical spectroscopy is used to study the non-equilibrium state of $Bi_2Sr_2CaCu_2O_{8+\delta}$ in the Normal state. Optical pump-probe technique is exploited in this thesis work. We measure the change in reflectivity $\Delta R/R$ which is proportional to the non-equilibrium quasiparticle density created by the pump laser pulse. Dependence of these measurements on absorbed pump fluence is obtained. We formulate the differential model starting from the Drude model to explain time-resolved reflectivity versus the wavenumber with relaxation rate γ_D and plasma frequency ω_P as free parameters. We report the dynamics of these parameters and their dependence on the absorbed pump fluence.

To my family ...

I wouldn't be at this stage without their support

(Sefi, Banch, Asse, Birsh, Messi, dani boy, John)

I love you all more than you can imagine

Acknowledgments

This thesis work wouldn't be possible without the help and support of the many peoples. In this short space it is difficult to mention all of them. But I would like to send my special acknowledgment to the following ones.

First and for most, I am very lucky and grateful to have Prof. Fulvio Parmigaini as an advisor for this thesis work. He has been supportive and excellent guider throughout this thesis work.

Giacomo Coslovich who train and teach me in the laboratory. He also let me use his basic experimental set-up for this thesis work. He is also the one gives a sense to everything I doubt about. Fedrico cliento who help me to understand the experimental set-up during my stay in the lab. I would like to thank all the rest group members of T-Rex.

A special thanks goes to the ICTP TRIL progmam for covering all expenses during my stay in Trieste.

Finally, my brothers and sisters provided me encouragement throughout my study; to my friends Dr. Gulilat, Yabe, and Tigist you have been my family in the last two years thank you for everything.

Table of Contents

1 Introduction **1**

1.1 Objective of this thesis 2

2 High Temperature Superconductivity **3**

2.1 Crystal Structure of Cuprates 3

2.2 Phase Diagram 4

2.3 Electronic properties of Cuprates 6

3 Optical Properties **11**

3.1 Static Optical properties 11

3.1.1 The Drude-Lorentz Model 11

3.1.2 Kramers-Kronig relations 15

3.1.3 Sum Rule 15

3.1.4 Static Data and Fit 17

3.2 Experimental Energy Scale 20

3.3 Time-Resolved Optical properties 22

3.3.1 Two-Temperature Model 23

3.3.2 Three-Temperature Model 25

3.3.3 Differential Reflectivity Model 26

4 Experimental Set-up **30**

4.1 Pump-probe technique 30

4.2 Laser system 31

4.2.1 Optical pump(Verdi V-18) 34

4.2.2 Laser Oscillator(Mira-seed) 35

4.2.3 Stretching and Compression Stage(Compressor/stretcher) . . . 37

4.2.4 The Laser amplification(RegA) 39
4.2.5 The Optical parametric Amplification (OPA) 40
4.3 Characheterization of pulses 43
4.3.1 Autocorrelation measurements 44
4.3.2 Cross-correlation measurements 45
4.3.3 Peak Power of OPA 46
4.3.4 Spatial beam profiles 47
4.4 Data Acquisition System and Main Improvements 48
4.4.1 Experimental setup using the Monochromator 48
4.4.2 Characterization of the Monochromator 49
4.4.3 Lock-in detection 51

5 Experimental Results 53
5.1 Tuneable wavelength pump-probe experiment 53
5.2 Linear Dependence of Differential Reflectivity on absorbed pump fluence 58
5.3 Pump-probe experiment with improved spectral resolution 58
5.4 Near-infrared and Supercontinuum Differential Reflectivity 59
5.5 Sign change dynamics dependence on Fluence 62

6 Data Analysis and Discussions of Results 65
6.1 Differential Reflectivity Fit 65
6.2 Fleunce Dependence of $\Delta\gamma_D$ and $\Delta\omega_p$ 67

7 Conclusion 69

References 70

List of Tables

3.1 Parameters used to fit the $\varepsilon_1(\omega), \varepsilon_2(\omega)$ and $R(\omega)$ 19

6.1 Results of the fit 66

List of Figures

2.1 Crystal structure of the cuprate compound Bi2212, showing the copper (purple) and oxygen (black) layer responsible for superconductivity. . 3

2.2 Generic and simplified doping dependent phase diagram of cuprates for both electron (n) and hole (p) doping. The phases shown are the antiferromagnetic (AF) phase close to zero doping, the superconducting phase around optimal doping, and the pseudogap phase. 4

2.3 The phase diagram of Bi-2212 based on transport and infrared measurements. The dashed line labeled T* is the boundary between the high-temperature strange-metal region and the pseudogap region. . . 5

2.4 (Left panel)CuO_2 planes made from CuO_4 squares sharing corner oxygens and (right panel) schematic view of the electronic layers in copper oxide superconductors. Taken from [1] 6

2.5 (a) Cu-O coordination polyhedra found in copper oxide superconductors.(b) d electron configuration for Cu21, (c)schematic picture of the energy states in copper oxide superconductors, and (d) split $d_{x^2y^2}$ band for interacting electrons in cuprates (UHB is upper Hubbard band and LHB is lower Hubbard band). 8

3.1 Optical conductivity of Bi-2212 at T_c and for T_c. 17

3.2 Temperature dependence of the screened plasma frequency ω_p for optimally doped (top) and underdoped (bottom) $Bi_2Sr_2CaCu_2O_{8-\delta}$.The calculated temperature dependence of plasma frequency 20

3.3 Bi2212 optimally doped data at 300 K reflectivity, real and imaginary parts of the dielectric function respectively(from top to bottom). The blue line is the fit and the green one is the data. 21

3.4 Characteristic energy scales in high-T_c superconductors. Infrared and optical spectroscopies allow one to probe electronic excitations in the frequency range from 20 cm^{-1} to at least 50,000 cm^{-1}. Several other techniques described in this section are suitable for extending the low-energy boundary down to microwave frequencies. 22

3.5 Results from solving the 2-T model with a Gaussian-shaped excitation pulse, illustrating the nonequilibrium heating conditions when the electron temperature(T_{el}) exceeds the phonon temperature (T_{ph}). Taken from [2]. 24

3.6 Sketch of the energy transfer during the relaxation process. Hot electrons generate hot phonons with characteristic time τ_α, while hot phonons dissipate their energy their energy on a time scale $\tau_\beta >> \tau_\alpha$. 26

3.7 The differential reflectivity model calculated by changing only the ω_P and γ_D. 27

3.8 The differential model: the different plots shown are made by slight change of ω_P with respect to the equilibrium value. The black arrows show the plots are with decreasing ω_P. 28

3.9 The differential model: the different plots shown are made by slight change of γ_D with respect to the equilibrium value. The black arrows show the plots are with increasing γ_D. 28

4.1 Typical schematic set-up of the pump-probe technique 31

4.2 Where the box in the top right corner represents the laser system which produces the 800 nm laser with a 250 kHz repetition rate; BS= the beam splitter has 10/90 reflectivity to transmitivity ratio; OPA = optical parametric amplifier; M1, M2, and M3 are the gold mirrors used to direct the pulses to the sample where M4 and M5 are used to direct it on the photo diode; PD= photo diode; SM (f=30 cm)= spherical lens used to focus the probe on the sample; L1 (f= 40 cm) = lens used to focus the pump pulse on the sample; L2 (f = 12.5 mm) = used to collect the reflected probe from the sample. L3 (f=7.5 mm) = used to focus the reflected probe on the entrance slit of the M266 monochromator PC = the computed used to display the signal. . . . 32

4.3 Optical set-up without the Monochromator. The only difference from figure 4.2 is that, this setup is with out the monochromator. 33

4.4 The Laser source 34

4.5 Mira seed oscillator 35

4.6 Group velocity dispersion compensation 36

4.7 The self-focusing of a laser beam in a medium with n2 $>$ 0 37

4.8 Kerr lens mode-locking 37

4.9 Expander-Compressor layout 38

4.10 Schematic layout of a grating-based compressor. where the long-wavelength shown in red and the short-wavelength shown in blue. 38

4.11 Schematic layout of a grating-based stretcher. 39

4.12 RegA Q-switch operation 39

4.13 The schematic view of the RegA seeded operation. Taken from [3] . . 40

4.14 The pulse build up in the RegA seeded operation 40

4.15 The RegA amplification layout 41

4.16 The layout of the OPA 42

4.17 Internal look of the autocorrelator. 44

4.18 Shows the figure taken form autocorrelator of 800 nm pulse duration 45

4.19 Cross-correlation measurements on the different wavelength of the probe pulse 46

4.20 The pulse width from cross-correlation measurements versus the wavelength of the probe beam. Where the horizontal red line shows the pulse width of the 800 nm. 47

4.21 The signal and the idler power of the OPA versus the wavelength . . 47

4.22 Shows the spot size of the pump and probe beam. Where the left side is the probe while the right side is called the pump. 48

4.23 Exact M266 monochromator from solar laser systems. 49

4.24 The Monochromatized signal ploted with the broad OPA pulse 50

4.25 Measurement of the OPA signal in the narrow band by putting inteference filter infront of the entrance slit 50

4.26 The Lock-in Detection system 52

5.1 The graph is 2D matrix plot at $\phi \sim 892\ /cm^2$ in spectral range of 4166.67 - 9174.31 cm^{-1}. A horizontal white line present in the plot is due to the OPA laser source gives too low signal in that spectral range. 54

5.2 Single scan measurement at fixed wavelength and the inset plot is the measurement near the sign change point. 55

5.3 The graph is 2D matrix plot at $\phi \sim 44.6\ /cm^2$ in spectral range of 4166.67 - 9174.31 cm^{-1}. A horizontal white line present in the plot is due to the OPA laser source gives too low signal in that spectral range. 56

5.4 Single scan measurement at fixed wavelength 56

5.5 The fit of single scan measurement at 2080 nm wavelength. 57

5.6 The reflectivity variation versus the wavenumber at different delay time in the spectral range of about 4000-9000 cm^{-1} ($\phi \sim 892\ /cm^2$). . . . 57

5.7 The reflectivity variation versus the wavenumber at different delay time in the spectral range of about 4000-9000 cm^{-1} ($\phi \sim 44.6\ /cm^2$). . . . 58

5.8 Reflectivity variation measurments at different absorbed pump intensities for the in Normal (300K). 59

5.9 Dependence of the absorbed pump intensity versus maximum value of the reflectivity variation 59

5.10 The upper graph 2D matrix of single wavelength scans measurments shown in Lower plot in spectral range of 1140 - 1320 nm ($\phi \sim 624.94$ $/cm^2$). 60

5.11 The upper graph 2D matrix of single wavelength scans measurments shown in Lower plot in spectral range of 1220 - 1400 nm ($\phi \sim 624.94$ $/cm^2$). 61

5.12 The reflectivity variation versus the wavenumber at zero delay time in spectral range of 1140 - 1320 nm ($\phi \sim 624.94$ $/cm^2$). 62

5.13 The near-infrared and supercontinuum probe fitted with the differentail model. 63

5.14 $\Delta R/R$ =0 at different absorbed pump fluence in Normal state (300K). 64

5.15 Dependence of the absorbed pump intensity versus sign change point of $\Delta R/R$ 64

5.16 Shows the sign change point decay fitted with the double exponential function. 64

6.1 Time-resolved reflectivity of both the IR and SC data with the differential fit. 65

6.2 Differential reflectivity data and the fit in the 4166.67 - 9174.31 cm^{-1} spectral region. 66

6.3 The calculated γ_D value (the red circles) and the fit with a three temperature model (in the blue lines). 67

6.4 The calculated ω_p value (the red circles) and the fit with a three temperature model (in the blue lines). 67

6.5 Linear dependence on the absorbed pump fluence of the calculated change of Drude gamma at each instant of the delay time. 68

6.6 Power law dpendence on the absorbed pump fluence of the calculated plasma frequency at each instant of the delay time. 68

CHAPTER 1

Introduction

The first high-temperature superconductor (HTSC) has been discovered by Bednorz and Müller in 1986[4]. Since then the question on how the superconductivity arises in these kind of materials have been puzzling for many scientists. The question remains open leading to strong debate in both theoretical and experimental condensed matter physics.

In conventional superconductors superconductivity arises below T_c due to the formation of condensed Cooper pairs thanks to the phonon mediated electron-electron attraction. The Bardeen-Cooper-Schrieffer theory (BCS theory) satisfactorily explains this phenomena. The origin of Cooper pairs formation in HTSC is still unknown. In the normal state of these systems electron-electron interactions plays a major role and thier electronic structure can not be explained within the independent electron approximation.

In recent years different techniques have been used to investigate the effect of low-energy excitation in the electronic structure of cuprates. The major breakthrough in the last decade was the discovery of the d-wave symmetry superconducting gap by microwave spectroscopy[5], evidence of electronic inhomogeneity by Scanning tunneling spectroscopy (STS)[6] and the existance of the pseudo gap above the T_c [7].

Time-resolved techniques have recently opened a way to study the optical properties in non-equilibrium conditions on a time scale of femtosecond. Separating the optical response of electrons, electronic excitations and phonons[8]. This technique can address the core issue of the delicate interplay between electron-electron and electron-phonon interaction in HTSC.

In aim of this thesis is to study the time-resolved optical properties of optimally

doped $Bi_2Sr_2CaCu_2O_{8+\delta}$ (Bi2212) in the strange metal phase (T=300K). We exploit a pump-probe experimental technique: first the non-equilibrium state is prepared by the absorption of a short pump laser pulse of 50 fs pulse duration at an eneregy of 1.5 eV. The pump pulse perturbs the density and energy distribution of quasiparticles and then the second tunable probe pulse is used to measure the recovery dynamics of the system by time-resolving the changes in the optical response functions of the medium that take place after photoexcitation.

The thesis is organized in the following way: Chapter 2 include the discussion on general properties of HTSC and in particular for Bi2212 optimally doped. Chapter 3 presents the static optical properties and the differentail model here developed. Chapter 4 is about the experimental set-up, i.e. laser source, characterization of pulses, pump-probe technique and the main improvements in data acquisition. In chapter 5 we report the main experimental results of this thesis. Chapter 6 is devoted to the data analysis and discussion. Finally, Chapter 7 includes the conclusive remarks of this thesis.

1.1 Objective of this thesis

The objective of this thesis is to address the following topics:

1. Experimental study of the dynamical optical properties in the intra-band spectral region of Bi2212 optimally doped.

2. Formulation of the differential model to interpret time-resolved reflectivity spectra.

3. Study of the interplay between Drude electrons lifetime and the plasma frequency.

CHAPTER 2

High Temperature Superconductivity

In this chapter we are going to review some of the important properties of high tempererature superconductors such as the Crystal structural, phase diagram and electronic properties of cuprates including the theoretical porposals to explain the properties of undoped or parent compound.

2.1 Crystal Structure of Cuprates

HTSC adopt layered perovskite structure. It contain CuO_2 plane bridged by cation layer, whereas groups of CuO_2 planes are separated with layers containing oxygen ions together with cations of various elements. Neighboring layers containing ions such as Bi and Sr are useful to stabilize the structure of doped electrons or holes onto the copper-oxide layers. These ions act as charge reservior [9].

Figure 2.1 showns the unit cell of Bi2212. The dimensions of the unit cell in the c-axis vary strongly depending on the number of CuO_2 layers, whereas in a or b axis directions the lattice parameters are fairly constant $\approx$5.4 A°.

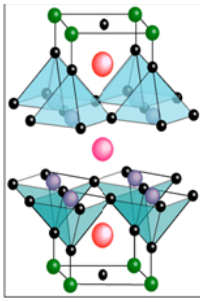


Figure 2.1: Crystal structure of the cuprate compound Bi2212, showing the copper (purple) and oxygen (black) layer responsible for superconductivity.

The Bi2212 is double-layered system, which means it contains n=2 CuO_2 planes in the unit cell. The electron transport and processes responsible for superconductivity in HTSC are believed to be intimately connected to CuO_2 planes.

2.2 Phase Diagram

High temperature superconductivity is achieved when a moderate density of electrons or holes is introduced into the parent antiferromagnetic of the cuprates. This is called Doping. Doping usually removes electrons from the electrically active CuO_2 crystal planes containing copper and oxygen atoms, although sometimes doping add electrons to the planes. Figure 2.2 shows schematic picture of possible doping ranges for some common compounds. The doping can be p-type (hole doped) the right side from the T=0 axis point while the other side is n-type (electron doped).

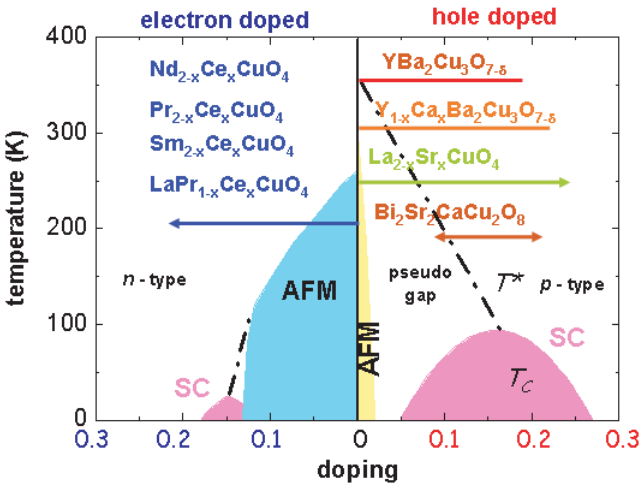


Figure 2.2: Generic and simplified doping dependent phase diagram of cuprates for both electron (n) and hole (p) doping. The phases shown are the antiferromagnetic (AF) phase close to zero doping, the superconducting phase around optimal doping, and the pseudogap phase.

Figure 2.3 shows the temperature-doping phase diagram of Bi2212 based on transport and IR measurements. The highest-temperature region designated in the diagram is the *strange-metal region*. This region is characterized by linear ab-plane resistivity and a linear scattering rate variation with frequency. The interplane con-

ductivity is frequency independent in this region. Below the strange metal phase is the pseudogap region. The resistivity in the c-axis direction develops a semiconducting dependence in this region, and the line separating the two regions has been based on c-axis transport measurements. The dashed line separating the pseudogap region from the coherent region has been based on recent ab-plane infrared data. Finally, the lowest temperature region is that of long-range superconductivity. The line separating it from the normal state is the parabolic approximation.

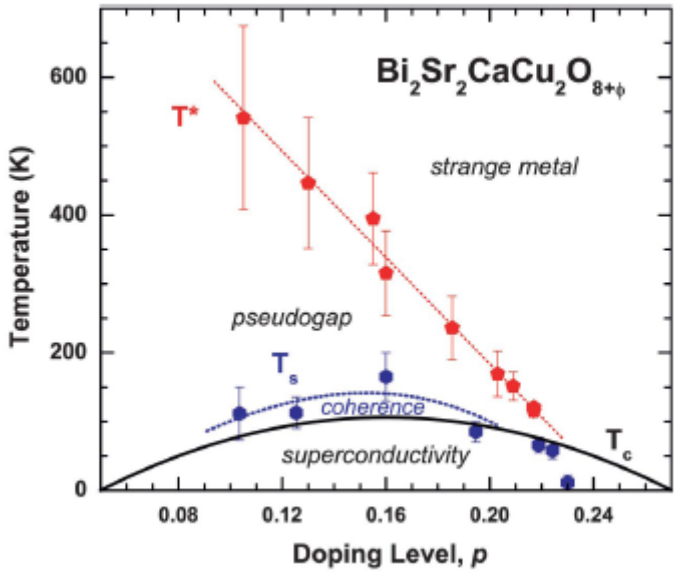


Figure 2.3: The phase diagram of Bi-2212 based on transport and infrared measurements. The dashed line labeled T* is the boundary between the high-temperature strange-metal region and the pseudogap region.

In superconducting region with the maximum critical temperature (T_c) reached at $\delta \approx 0.15$ value which is called *optimal doping*. The region of doping level $\delta < 0.15$ is called *underdoped* whereas the $\delta > 0.15$ is called overdoped. For the hole concentration greater than $\delta = 0.25$ the superconductivity vanishes and acts like a metal.

A variety of physical probes reveal a captivating feature of this state, a partial or incomplete gap already in the normal state that resembles the superconducting gap, in both magnitude and symmetry, leading to a view accepted by many theoreticians and experimentalists that the origin of the pseudogap may be intimately related to

superconducting pairing at $T < T_c$. An alternate point of view holds that the pseudogap represents a state that competes with superconductivity. Infrared spectroscopy has an outstanding track record in probing various gapped states in solids, and this research has provided important contributions to the experimental picture of the pseudogap state in cuprates.

2.3 Electronic properties of Cuprates

All Cuprates contain at least one CuO_2 conducting planes in the unit cell. The copper-oxide planes are checkerboard lattices with squares of O^{2-} ions with a Cu^{2+} ion at the centre of each square (see figure 2.4(left panel)). Each copper atom forms a bond with six oxygen atoms four of them are on the CuO plane and the rest two are above and below the CuO plane. As it shown in figure 2.4(right panel) above and below the CuO planes there are other ions and act as a charge reservoir (**CR**) can accept or donate electrons to CuO planes [1].

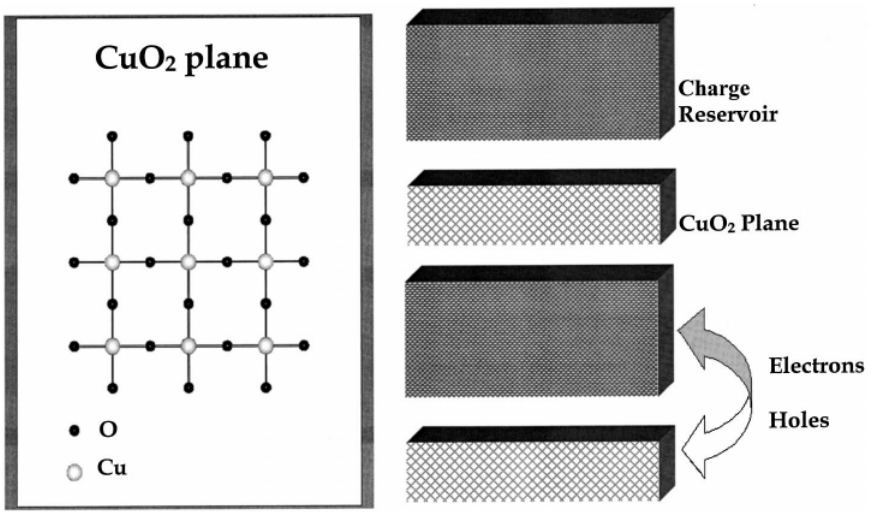


Figure 2.4: (Left panel)CuO_2 planes made from CuO_4 squares sharing corner oxygens and (right panel) schematic view of the electronic layers in copper oxide superconductors. Taken from [1]

From band theory calculations the undoped cuprate material indicate that it should be metallic, but in reality it is insulating. The result is not a failure of the

details of the calculations it is just because of the chemical valency considerations also imply that it should be metalic. The electronic confugration of the undoped cuprate material has an odd number of electrons per unit cell this results half filled valence band. Looking at the electronic configuration of the each element in the CuO_2 compound.

- Cu = [Ar]$4s^1 3d^{10}$
- O = [He]$2s^2 2p^4$

The electronic confugration of the Cu^{2+} ions that form the basis for the superconducting compounds is: [Ar]$3d^9$ nine of the ten available d-orbital energy states are filled. In the $Cu-O$ coordination polyhedra (octahedra, pyramids, and squares) that form in the cuprate superconductors, these energy levels are nondegenerate. The oxygen 2p orbitals, which are directed between the oxygen atoms, are at low energy and, therefore, are completely filled with six electrons. The shapes of the $Cu-O$ coordination polyhedral are such that there are four near in-plane oxygen neighbors and one (pyramidal) or two (octahedral) apical oxygens more distant when present. This makes the energies of the orbitals with z components (i.e. toward the apices) because of lower repulsion from the oxygen orbitals. This results that the nine electron configuration has a single unpaired electron in the $d_{x^2-y^2}$ orbital (see Figure 2.5(b)), which points toward the in-plane oxygens. The single unpaired electron carries a spin of $1/2$.

In isolated atoms these orbitals are discrete energy states but in solids, where the atoms are close together, the orbitals interact, and the sharp atomic energy states become bands of energies. The similar energy of the O 2p states and the Cu 3d states leads to the situation shown in figure 2.5(c). The electrons fill half of the Cu $d_{x^2y^2}$-derived band, and the high-energy part of the oxygen derived band has almost the same energy as the highest occupied copper states. This is more complicated than in the usual electronic oxides, but the complexity continues. This type of picture would predict that Cu^{2+} oxides with the superconducting structure types should be metallic conductors. They are, instead, electrical insulators. The standard picture

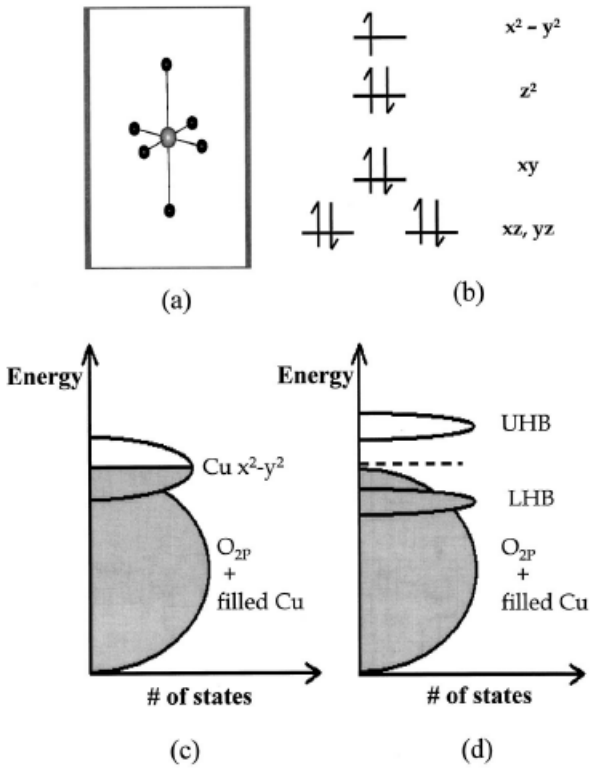


Figure 2.5: (a) Cu-O coordination polyhedra found in copper oxide superconductors.(b) d electron configuration for Cu21, (c)schematic picture of the energy states in copper oxide superconductors, and (d) split $d_{x^2y^2}$ band for interacting electrons in cuprates (UHB is upper Hubbard band and LHB is lower Hubbard band).

for the electronic properties of solids assumes that the electrons are not interacting with each other, only with the underlying atomic lattice. In the copper oxides, this is not the case and they do interact.

The interaction between electrons is greatest in half-filled bands, which is exactly the case for the cuprates. The addition of the second electron to the $d_{x^2y^2}$ orbital takes a significant amount of extra energy, because it is repelled by the electron already present (called on-site repulsion energy). The reason is that the energy states for the second electron are higher than the first electron, and there is a gap of non allowed energies between the two. The bandgap between the highest occupied oxygen states and the empty part of the Cu $d_{x^2-y^2}$ band (see figure 2.5(d)) is what leads to the insulating behavior.

The electronic structure of CuO_2 plane is described by models generalizing the Hubbard Hamiltonian. The Hubbard mechanism splits the Cu d-band into two i.e. upper and lower Hubbard band (see from the figure 2.5 (d)) due to a large correlation gap of 8 eV because of strong Coulomb repulsion(U) on Cu $d_{x^2-y^2}$ [10]. The highest occupied band (sometimes referred to as charge-transfer band) is about 1.7 eV below the upper Hubbard band and is derived from predominantly O 2p-bands and the fillled Cu d-band.

The Hubbard Hamiltonian has two components the first component is the hopping integral. The hopping integral is typically represented by the letter t because it represents the kinetic energy of electrons hopping between atoms. The second term in the Hubbard model is then the on-site repulsion, typically represented by the letter U because it represents the potential energy arising from the charges on the electrons. Can be written in second quantization notation, the Hubbard Hamiltonian then takes the form:-

$$H = -\sum_{ij}\sum_{\sigma} t_{ij} C_{j\sigma} C^{+}_{i\sigma} + \frac{1}{2}\sum_{ijkl}\sum_{\sigma\sigma,} \langle ij|U|kl\rangle \, C^{+}_{i\sigma} C^{+}_{j\sigma,} C_{l\sigma,} C_{k\sigma} \tag{2.1}$$

where $\sigma = \uparrow, \downarrow$ is spin index here we consider only spin 1/2 fermions, $C_{k\sigma}=$ are fermions annihilation operators, $C^{+}_{k\sigma}$ the complex conjugate is creation operator, and t_{ij}=represents the hopping integral between sites i and j while U is a two body

potential (e.g. coulomb).

$$t_{ij} = \begin{cases} t, & \text{if (i,j)} for Nearest Neighbour \\ 0, & \text{otherwise} \end{cases} \tag{2.2}$$

And the interaction potential

$$\langle ij|U|kl\rangle = \begin{cases} U, & \text{if i=j=k=l} \\ 0, & \text{otherwise} \end{cases} \tag{2.3}$$

Now for the Nearest neighbor and for the case of $i = j = k = l$ the hamiltoniam of one band Hubbard model simplifies to

$$H = -t \sum_{i} \sum_{\sigma} C^{+}_{i\sigma} + \frac{U}{2} \sum_{\sigma\sigma,} C^{+}_{i\sigma} C^{+}_{i\sigma,} C_{i\sigma,} C_{i\sigma} \tag{2.4}$$

CHAPTER 3

Optical Properties

In the first section we present discussion of classical model (i.e Drude-lorentz model) used to describe the optical properties of cuprates at 300K. Then we report the static optical reflectivity data of optimally doped $Bi_2Sr_2CaCu_2O_{8+\delta}$ in the normal state.

In the second section we introduce the theoretical models that are essentional to give the physical interpretaion of the time-resolved reflectivity measurement data. Finally, the formalism of the differential model that we propose using the classical approach is presented.

3.1 Static Optical properties

The classical treatment of interaction of radiation with solids can be explain based on the Lorentz and Drude oscillators[11]. The Lorentz model is applicable to insulators, since it describes all direct interband transitions i.e. all transitions for which the final state of an electron lies in a different band but with no change in k- vector in the reduced zone scheme. The Drude model is applicable to free electron metals by considering only the intraband transitions i.e. all the transitions within the same band which is not involving in a reciprocal space. The lorentz and Drude model are good starting points to model the optical properties of solids.

3.1.1 The Drude-Lorentz Model

The Lorentz model is used to describe frequency dependent polarization due to bound electrons to the atom core. This oscillator allowed us to model materials which has optical properties are dominated by a single resonance frequency (or absorption line).

To derive the mathematical equation of the Lorentz model we consider the motion of an electron bound to the nucleus and described by the equation.

$$m\frac{d^2\mathbf{r}}{dt^2} + m\gamma\frac{d\mathbf{r}}{dt} + m\omega_0^2\mathbf{r} = -eE_{loc} \tag{3.1}$$

Where m is the electronic mass, e is the magnitude of the electronic charge, E_{loc} is the local electric field acting on the electron as a driving force, $m\gamma\frac{d\mathbf{r}}{dt}$ represents viscous damping and provides energy loss mechanism, and $m\omega_0^2\mathbf{r}$ is the restoring force.

To reach on equation(3.1) we make two approximations first one is the nuclues has infinite mass and the second one is we neglect the force $(-e\mathbf{v}\text{ x }\frac{\mathbf{B}}{c})$ coming out of the the interaction of the electron with the magnetic field of the electromagnetic wave it is because the velocity of the electron is very small compared with c.

Solving the second order differential equation by considering the local field is time varing in the form of phase $e^{-i\omega t}$ then the solution of 3.1 becomes

$$\mathbf{r} = \frac{-eE_{loc}}{m}\frac{1}{(\omega_0^2 - \omega^2) - i\gamma\omega} \tag{3.2}$$

and the induced dipole moment $(\mathbf{P} = -e\mathbf{r})$ is

$$\mathbf{P} = \frac{e^2E_{loc}}{m}\frac{1}{(\omega_0^2 - \omega^2) - i\gamma\omega} \tag{3.3}$$

Since the displacement r is small a linear relationship is exist between P and E_{loc}

$$\mathbf{P} = \alpha(\omega)E_{loc} \tag{3.4}$$

Where $\hat{\alpha}(\omega)$ is the frequency-dependent atomic polarizability. Comparing equation 3.3 and 3.4 we find the equation for the polarizability

$$\alpha(\omega) = \frac{e^2}{m}\frac{1}{(\omega_0^2 - \omega^2) - i\gamma\omega} \tag{3.5}$$

The polarizability is complex because of the damping term. As a result, the polarization differs in phase from the local field at all frequencies. If there are N atoms per unit volume, the macroscopic polarization is

$$\mathbf{P} \ = N\langle p\rangle = N\alpha\langle E_{loc}\rangle = \chi_e\mathbf{E} \tag{3.6}$$

Where χ_e is the electric susceptibility. We make also an assumption by considering $\langle E_{loc} \rangle = E$; this equality is far from obvious. And the displacement is given by

$$\mathbf{D} = \varepsilon \mathbf{E} = \mathbf{E} + 4\pi N \mathbf{P} \tag{3.7}$$

Now from equation 3.5, 3.6 and 3.7 the dielectric function is given as following;

$$\varepsilon(\omega) = 1 + \frac{4\pi N e^2}{m} \frac{1}{(\omega_0^2 - \omega^2) - i\gamma\omega} \tag{3.8}$$

From equation 3.8 we can drive the Drude part dielectric function just by setting the $\omega_0 = 0$ we obtain

$$\varepsilon(\omega) = 1 - \frac{4\pi N e^2}{m} \frac{1}{\omega(\omega^2 - i\gamma)} \tag{3.9}$$

The origin of the γ in the Drude model for the free electron model is electron scattering. It is known that the damping term is the related to the mean free time between collisions by $\gamma = 1/\tau$. The τ depends linearly with temperature but it is independent of frequency in the Drude model. The dielectric function(ε).

$$\varepsilon(\omega) = 1 + \frac{\omega_p^2}{(\omega_0^2 - \omega^2) - i\gamma\omega} \tag{3.10}$$

Where N = number of atoms per unit volume, γ = the scattering rate, and $\omega_p^2 = \frac{4\pi N e^2}{m}$.

If we consider classical atoms with more than one electron per atom the dielectric function given in equation 3.10 modified in to

$$\varepsilon(\omega) = 1 + \frac{4\pi e^2}{m} \sum_j \frac{N_j}{\left(\omega_j^2 - \omega^2\right) - i\gamma_j\omega} \tag{3.11}$$

Where N_j be the density of electrons bound with resonance frequency ω_j and $N = \sum_j N_j$. The quantum mechanical version of this equation can be written as the following

$$\varepsilon(\omega) = 1 + \frac{4\pi N e^2}{m} \sum_j \frac{N f_j}{\left(\omega_j^2 - \omega^2\right) - i\gamma_j\omega} \tag{3.12}$$

Where ω_j is the transition frequency between two atomic states separated by $\hbar\omega_j$ and the parameter f_j is the oscillator strength is the measure of the relative probability of a quantum mechanical transition. The sum rule for f is given by

$$\sum_j f_j = 1 \tag{3.13}$$

Considering the frequencies out of the frequency range the dielectric function is written as the following form, which is called the Drude-Lorentz model.

$$\varepsilon(\omega) = \varepsilon_\infty + \sum_j \frac{\omega_{pj}^2}{\left(\omega_j^2 - \omega^2\right) - i\gamma_j\omega} \tag{3.14}$$

Where ε_∞ is called the 'High-frequency dielectric constant', which represents the contribution of all oscillators at high frequencies (compared to the frequency range under consideration).

The complex dielectric function and the complex conductivity can be written in the similar way

$$\varepsilon = \varepsilon_1(\omega) + i\varepsilon_2(\omega) \tag{3.15}$$

and

$$\sigma = \sigma_1(\omega) + i\sigma_2(\omega) \tag{3.16}$$

The real and imaginary parts of the dielectric function and the conductivity are related by a couple of simple equations

$$\begin{cases} \sigma_1(\omega) = (\omega/4\pi)\,\varepsilon_2(\omega) \\ \\ \sigma_2(\omega) = -(\omega/4\pi)\,[\varepsilon_1(\omega) - 1] \end{cases} \tag{3.17}$$

The Drude optical conductivity $\sigma(\omega)$ derived from equation 3.17.

$$4\pi\sigma(\omega) = \frac{\omega_p^2}{1/\tau - i\omega} \tag{3.18}$$

In experiments the measured quantity is the reflectivity from solids so the relation between dielectric function and the reflectivity is very crucial to understand the results. The equation that relates ε and the reflectivity at the normal incidence is given by the following formula

$$R = \left|\frac{1 - \sqrt{\varepsilon}}{1 + \sqrt{\varepsilon}}\right|^2 \tag{3.19}$$

The refractive index $n^2(\omega) = \varepsilon(\omega)$ so equation 3.19 can be rewritten as

$$R = \frac{(n_1 - 1)^2 + (n_2)^2}{(n_1 + 1)^2 + (n_2)^2} \tag{3.20}$$

3.1.2 Kramers-Kronig relations

The principle of causality due to an electromagnetic field states that dielectric function can be splitted as a real and imaginary parts.

$$\varepsilon(\omega) = \varepsilon_1(\omega) + i\varepsilon_2(\omega) \tag{3.21}$$

Where ε_1 is real and ε_2 is the imaginary parts of the dielectric function. The two parts of the dielectric function are not independent one from the other but they are related by the Kramers and Kroing (KK) dispersion relations. The KK relations are written as:

$$\varepsilon_1(\omega) = 1 + \frac{2}{\pi} P \int_0^\infty \frac{\omega' \varepsilon_2(\omega')}{\omega'^2 - \omega^2} d\omega' \tag{3.22}$$

And

$$\varepsilon_2(\omega) = -\frac{2\omega}{\pi} P \int_0^\infty \frac{\varepsilon_1(\omega') - 1}{\omega'^2 - \omega^2} d\omega' \tag{3.23}$$

Where P indicates that we have to take the principal values of the integral since we are doing the integration on the complex plane.

3.1.3 Sum Rule

The dissipative part of the dielectric function satisfies the so-called sum rule. The sum rule satisfy integral relation of quantities that are constant during temperature changes. The origins of sum rules are related to conservation laws and causality of the response functions. The implications of sum rule more importantingly, the global oscillator strength sum rule which is related to the integral of the imaginary part of dielectric function [12].

$$\int_0^\infty \omega \varepsilon_2(\omega)\, d\omega = \frac{2\pi^2 n e^2}{m_e} \tag{3.24}$$

Where e the charge of electron, m_e the electron mass, and n the number of electrons per unit volume involved in the interaction with the electromagnetic wave. The integral of equation 3.24 is a measure of the energy absorption for all frequencies.

The sum is frequently defined in terms of the effective number of electron per atom(n_{eff}) contributing to the optical properties over finite range. Equation 3.24

can be written as

$$\int_0^{\omega_c} \omega\varepsilon_2(\omega)\, d\omega = \frac{1}{2}\pi \left(\frac{4\pi^2 N_\alpha e^2}{m_e}\right) n_{eff}(\omega_c) \tag{3.25}$$

Where N_α is the density of atoms. There is another sum rule which is related to plasma excitations. The integration to infinite frequency in Eq 3.24 can rarely be exercised because of experimental constraints[13].

The sum rule has several applications here we will mention some of them. The first one is the integral can be limited to a finite range of the frequency in the electronic band width of w. Then equation 3.24 modified to

$$\int_0^{w} \omega\varepsilon_2(\omega)\, d\omega = \frac{2\pi^2 n e^2}{m_b} \tag{3.26}$$

This is called the partial sum rule. Where m_b is the band mass and is different from the free-electron mass.

The second application of sum rule is it can be applied to metals and can tell us information about an effective number of carriers contributing in the spectral weight. Since the sum in the infinite frequency range we can define spectral weight(SW) and the value is given by the formula 3.28. It remains constant as long as the integral is till infinity.

$$SW = \int_0^{\infty} \sigma_1(\omega)\, d\omega \tag{3.27}$$

The third application of sum rule is in cuprates. When we brought the HTSC below the critical temperature the electrons form a superfluid condensate. This results a condensate in the optical conductivity as a delta function at zero frequency. At the same time a gap opens up in low frequency part of the spectrum where the optical conductivity is close to zero (see figure 3.1). In the $T \geq T_c$ or in the normal state the conductivity is characterized by the Drude peak. To estimate precisely the contribution of the superconducting condensate the best way out is taking the difference in spectral weight between the optical conductivity in the superconducting and normal state. This is called Ferrel-Glover-Tinkham (FGT) sum rule.

$$SW = SW_{inter} + SW_{intra} = \int_0^{\infty} \sigma_1(\omega)\, d\omega \tag{3.28}$$

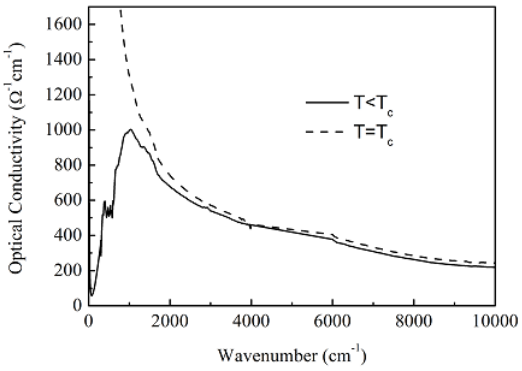


Figure 3.1: Optical conductivity of Bi-2212 at T_c and for T_c.

3.1.4 Static Data and Fit

In this section we report the in-plane reflectivity data of Bi2212 optimally doped in the normal state (300 K). These measurements have been performed by Dirk van der Marel's group by using different techniques, in order to cover all the spectral range between 50 cm^{-1} and 36000 cm^{-1} . The data between 6000 and 36000cm^{-1} have been collected with spectroscopic ellipsometry, whereas the infrared region of the spectrum was measured through reflectivity at normal incidence[14].

A simpler and more realistic picture the optical conductivity of the cuprates is a contribution of several simultaneously present features. The first contribution peaked at zero frequency, exhibits a lineshape strongly dependent on temperature, varies linearly with temperature [15]. It is well described by a Drude absorption where γ is independent of the ω.

The two mid-infrared(MIR) peaks in the interband region are centered ($\approx 0.5, 0.8$ eV) are represented by the lorentz oscilator. The origin and the physical process behind the MIR peaks are still debated [12], in the normal state the possible explanation could be transitions quasiparticles from the low-Habbard band(LHB).

The next two oscilators (i.e. $\approx 1.45, 2$ eV) are related to charge transfer transitions. These are transitions of a hole from the Cu $d_{x^2-y^2}$ band to the fermi energy in the $O-2P$ orbital [15]. The rest six lorentz oscilators centered at ($\approx$ 2.7, 3.85, 4.35, and 5 eV) are for the interband transitions.

By taking in to account all the above mentioned results and including the electronic transitions at higher frequencies we can model the optical conductivity of the cuprates at 300 K by means of the Drude term plus n Lorentz oscillators peaked at non-zero frequencies $\omega_j (j = 1, ..., n)$. We obtain

$$\sigma(\omega) = \frac{ne^2\tau}{[m^*(1 - i\omega\tau)]} + \frac{\omega}{4\pi i}\sum_{j=1}^{n}\frac{f_j\omega_j^2}{\left(\omega_j^2 - \omega^2 - i\omega\gamma_j\right)} \tag{3.29}$$

To summarize the contributions to the dielectric function of all families of the HTSC in the normal state, can be generalized using the following equation.

$$\varepsilon(\omega) = \varepsilon_\infty - \frac{\omega_p^2}{\omega^2 + i\omega\gamma_D} + \sum_j \frac{\omega_{p,j}^2}{\left(\omega_j^2 - \omega^2\right) - i\gamma_j\omega} \tag{3.30}$$

Where equation 3.30 contians ε_∞ is the High-frequency dielectric constant, Drude part peaked at zero frequency with ω_p plasma frequency and width γ_D and the inter-band tansitions are repreasented by the lorentz oscilators.

From the result of published paper by Molegraaf [14] the ω_p are temperature dependent. The plasma frequency decreases as square of temperature (see figure 3.2). Classically, temperature dependence of the $1/\tau$ is linear and increasing. These two results are important to fit the differential reflectivity data.

The static reflectivity (R) can be derived from the dielectric function as can be seen in equation 3.31. Using the two models i.e. the Lorentz and the Drude model the idea is to discuss the static optical properties of the High Tc superconductors.

$$R = \left|\frac{1 - \sqrt{\varepsilon(\omega)}}{1 + \sqrt{\varepsilon(\omega)}}\right|^2 \tag{3.31}$$

We can use the dielectric function as an input to calculate the reflectivity in wide range of frequencies and we can understand the electronic structure of cuprates.

In figure 3.3 the solid line is the fit to the data. The fitting function is the result of Drude term and several bound Lorentz oscillator each of them corresponds to the electronic structure of the cuprates. This kind of modeling enables to understand the effect of each oscillator on the total dielectric function and reflectivity. From the reported data we note that below 10000 cm^{-1} ($\approx$ 1.25 eV) the dielectric function is

Table 3.1: Parameters used to fit the $\varepsilon_1(\omega), \varepsilon_2(\omega)$ and $R(\omega)$

	parameters	T=300 K (cm^{-1})
Extended Drude	ε_∞	2.62
	ω_p	16901
	γ_{imp}	625
Mid-infrared peak	ω_0	4264
	ω_{p0}^2	22041800
	γ_0	4069
	ω_1	6789
	ω_{p1}^2	8142014
	γ_1	3925
Interband transitions	ω_2	11650
	ω_{p2}^2	5307060
	γ_2	3500
	ω_3	15409
	ω_{p3}^2	45542000
	γ_3	8905
	ω_4	21300
	ω_{p4}^2	223159025
	γ_4	13898
	ω_5	30756
	ω_{p5}^2	320536896
	γ_5	6908
	ω_6	678934946
	ω_{p6}^2	214474009
	γ_6	6396
	ω_7	40421
	ω_{p7}^2	756372000
	γ_7	7518

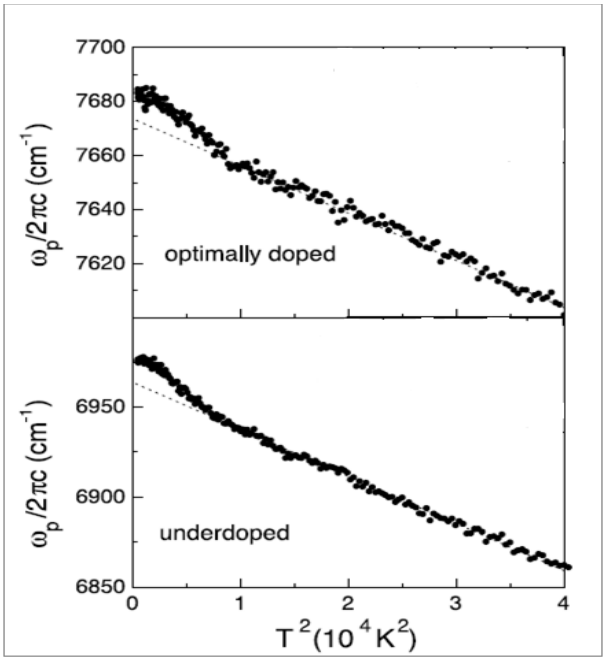


Figure 3.2: Temperature dependence of the screened plasma frequency ω_p for optimally doped (top) and underdoped (bottom) $Bi_2Sr_2CaCu_2O_{8-\delta}$.The calculated temperature dependence of plasma frequency

characterized by a Drude-like response. The fitting is done based on minimizing of the χ^2 value.

Conventional Drude model successfully accounts for the room temperature spectrum of metallic cuprates [15]. The conventional Drude model describes the optical conductivity for non-interacting electrons with a asingle and frequency independent scattering rate. But in the superconducting state of the Cuprates the scattering rate arises from the electron-electron and electron-phonon interactions and the scattering is both frequency and temperature dependent. In that kind of situation the conventional Drude model is insufficient. To overcome this problem we need to use *Extended Drude Model*[16, 17, 18, 19].

3.2 Experimental Energy Scale

As it shown in figure 3.4 the characteristic energy scales involved in the study of high-temperature superconductors. The IR and optical spectroscopy probe excitations and

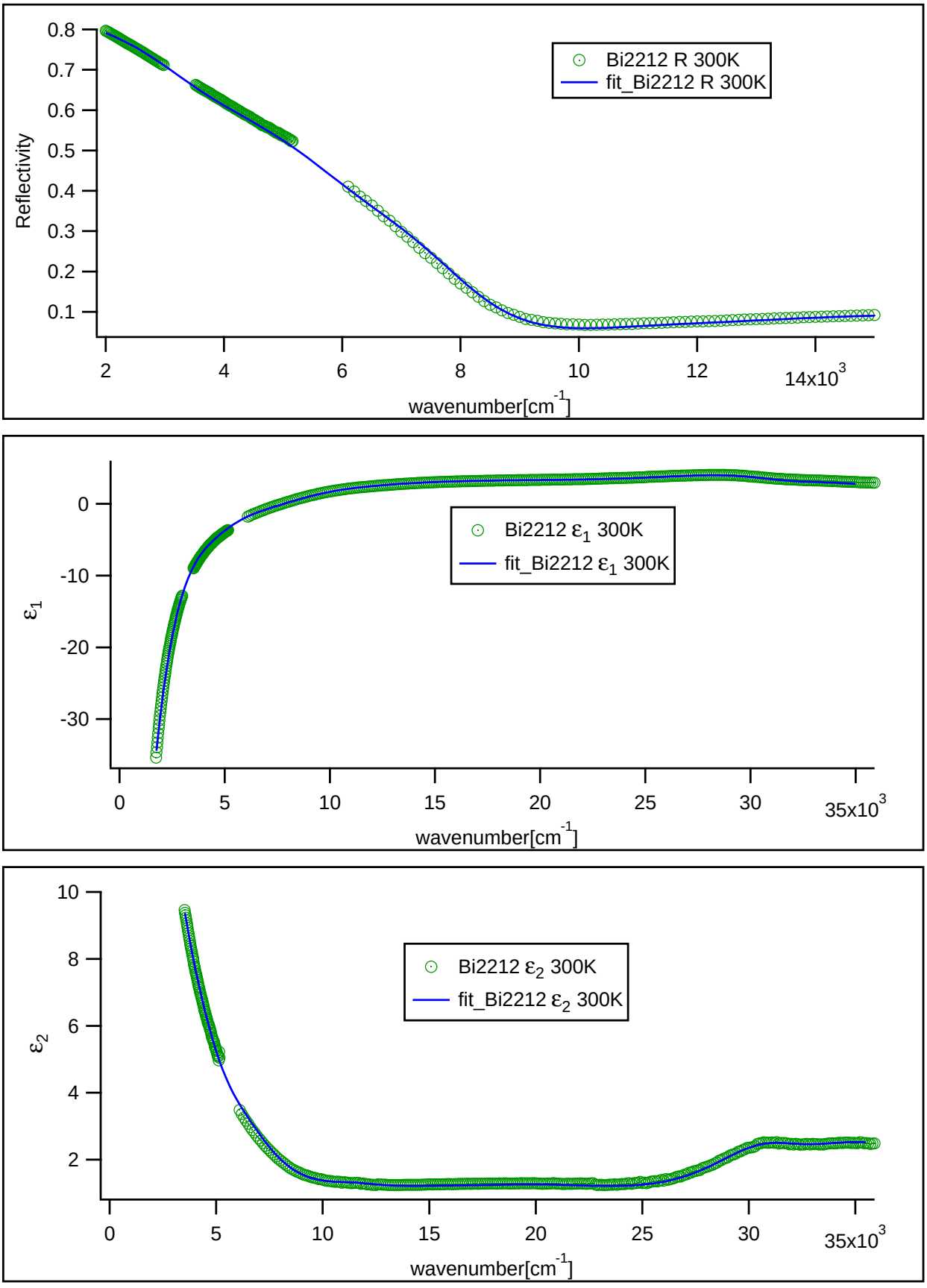


Figure 3.3: Bi2212 optimally doped data at 300 K reflectivity, real and imaginary parts of the dielectric function respectively(from top to bottom). The blue line is the fit and the green one is the data.

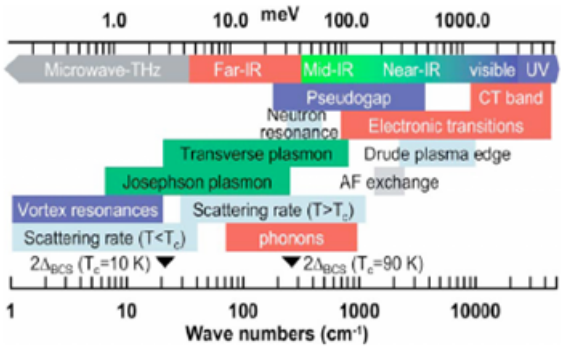


Figure 3.4: Characteristic energy scales in high-T_c superconductors. Infrared and optical spectroscopies allow one to probe electronic excitations in the frequency range from 20 cm^{-1} to at least 50,000 cm^{-1}. Several other techniques described in this section are suitable for extending the low-energy boundary down to microwave frequencies.

collective modes in the energy region from about 20 cm^{-1} (0.0024825 eV) up to 50 000 cm^{-1} (6.20625 eV).

The measurements in this thesis are collected in Near-infrared region is of special interest to superconductivity, since it includes both the electronic transitions, Drude plasma edge and the psuedogap region[13].

3.3 Time-Resolved Optical properties

Time-resolved optical reflectivity measurement is the result of photo-induced excitaion. We exploit pump-probe technique to study the relaxation dynamics of the quasi-particles in Normal state.

In this section we present the two and three temperature model to interpret the non-equilibrium dynamics in normal state Bi2212 optimally doped sample. We present also the formulation of differential model we propose in order to fit the differential reflectivity signal.

3.3.1 Two-Temperature Model

The two-temperature model (2T model) used for the first time by Anisimov for metals [20]. Later in 1987 Allen has used the this model to interpret the pump-probe measurements on metals [21].

Now let's describe the two temperature model: First the incident pump beam excite electrons in the conduction band while phonons are at eqiulibrium. This creates non-equilibrium electronic distribution results an increase of electron temperature T_{el} (electron thermalization). Electron-electron interactions control the attainment of a quasi-equilibrium electronic subsystem distribution at a characteristic relaxation rate $\gamma_{el} = \tau_{el}^{-1}$. Then the electrons start to interact with phonons until they reach to equilibrium. After the equilibruim point the temperature of electrons (T_{el}) decreases while the temperature of the phonons increases (T_{ph})(see figure 3.5). After some time the electrons and the phonons are in equilibrium, so the system has globally a temperature value higher than the initial one. Through heat diffusion from the surface to the substrate leads to the recovery of the initial temperature within several nanoseconds.

Phenomenologically, the physical picture two-temperature model can be described by the following two equations.

$$\begin{cases} C_{el}\frac{dT_{el}}{dt} = P_{in}(t) - g(T_{el} - T_{ph}) \\ \\ C_{ph}\frac{dT_{ph}}{dt} = g(T_{el} - T_{ph}) \end{cases} \tag{3.32}$$

Where C_{el}, C_{ph} are the electron and phonon specific heat respectively, P_{in} is the incident pump beam, $g = \gamma_{el-ph}.C_{el}$ represents the electron-phonon coupling constant and can be calculated from the Eliashberg function.

The electronic specific heat is defined as $C_{el} = \gamma_{el}.T_{el}$. The electron-phonon decay rate and the electron-phonon coupling constant are related by the equation 3.33, the formula is derived by Allen [22].

$$g = \frac{3\hbar\lambda\gamma\langle\omega^2\rangle}{\pi k_B} \tag{3.33}$$

Where γ_{el} is the coefficient of electronic specific heat and $\langle\omega^2\rangle$ is the distribution of

the frequency spectrum phonon and K_B is the boltzmann constant. Solving equation 3.30 we get time evolution of the electronic temperature (T_{el}). The value of τ_{el} is calculated by Allen 1987 [22].

$$\tau_{el} = \frac{\pi k_B T_{el}}{3\hbar\lambda \langle\omega^2\rangle} \tag{3.34}$$

The rise time of T_{el} in 2-T model is determined by the width of the incident pump laser pulse, while the decay rate (or fall time) is governed by the τ_{el-ph}. The electron-electron scattering rate time τ_{el} is generally considered very short, typically 100 fs or less, so the thermalization of the electron subsystem has usually been assumed to be an almost instantaneuos process [2, 23].

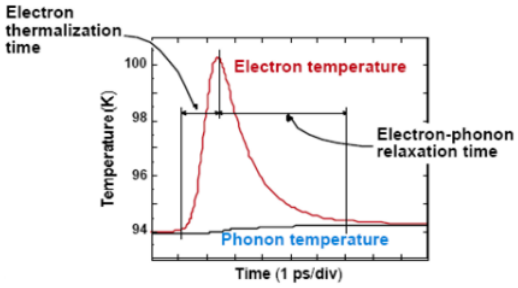


Figure 3.5: Results from solving the 2-T model with a Gaussian-shaped excitation pulse, illustrating the nonequilibrium heating conditions when the electron temperature(T_{el}) exceeds the phonon temperature (T_{ph}). Taken from [2].

The two temperature model also assumes that the change in reflectivity to be proportional to the change of electronic and lattice temperatures. So the variation of reflectivity measured is the measure of distribution of quasi-particles near the fermi level. For a thermalized non-equilibrium electrons with T_{el} we can say that $\Delta R \propto \Delta T_{el}$. The experimental justification is done by Rosei [24].

But this is not enough in reality we must also take in to account the temperature variation of lattice because the thermal expansion of the lattice and shift of the bands it results variation in optical properties. So the total variation of reflectivity becomes $\Delta R = A\Delta T_{el} + B\Delta T_{ph}$. Where A and B are constants. The part ΔR originated from the lattice ΔT varies in the time scale of longer than the diffussion of heat so it manifests as a change in the background of the ΔR signal. The variation of pulse

reflectivity is solely electronic effects if the sample is thin to limit the transport of heat which could affect the signal.

3.3.2 Three-Temperature Model

The three temperature model (3T model) is an extension of the two temperature model. It is a model used to interprete the differential reflectivity signal of superconductors. The model starts by considering the phonons have two subsets:

1. A limited number of modes, which interact more strongly with the electrons, and

2. A complementary subset of nearly noninteracting modes.

Electrons transfer energy to the phonons that are more strongly coupled with a characteristic time $\tau_\alpha = 110$ fs. Because of their small specific heat, this small subset of the total phonons acquires an effective temperature $T_p > T_l$. Already after τ=3τ_α=330 fs, the hot electrons and hot phonons reach a common temperature T_p $\cong$T$_e$=T_l +δT_e^β=300 fs, and the dynamics of hot electrons and hot phonons become similar. The electronic cooling can still proceed due to a residual scattering with the cold lattice modes. Moreover, we expect that hot phonons dissipate their energy by means of anharmonic decay. The relaxation by anharmonic cooling and scattering with cold phonons takes place with time constant τ_β=2 ps. After 3τ_β, the sample surface is in local equilibrium at $T_l = 60$ K. Heat diffusion from the surface to the substrate leads to the recovery to the intital temperature within several nanoseconds.

As can be seen from the figure 3.6 the 3T model has one extra intermediate process than in the 2T schematic figure 3.5. The rate equation of the three temperatures (i.e $T_e(\tau)$, $T_p(\tau)$, and $T_l(\tau)$) is given by three first order differential equations.

$$\begin{cases} \frac{\partial T_e}{\partial \tau} = -\frac{3\lambda\Omega_0^3}{\hbar\pi k_B}\frac{n_e - n_p}{T_e} + \frac{P}{C_e} \\ \\ \frac{\partial T_p}{\partial \tau} = \frac{C_p}{C_l}\frac{n_e - n_p}{T_e} - \frac{T_p - T_l}{\tau_\beta} \\ \\ \frac{\partial T_l}{\partial \tau} = \frac{C_p}{C_l}\frac{T_p - T_l}{\tau_\beta} \end{cases} \tag{3.35}$$

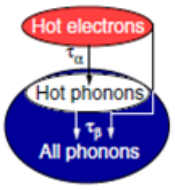


Figure 3.6: Sketch of the energy transfer during the relaxation process. Hot electrons generate hot phonons with characteristic time τ_α, while hot phonons dissipate their energy their energy on a time scale $\tau_\beta >> \tau_\alpha$.

Where P is the FWHM of the gaussian incident pump pulse, $C_e = \gamma T_e$, $C_p = 3f\Omega_0 \frac{\partial n_p}{\partial T_p}$ and $C_l = 3(1-f)\frac{\partial n_p}{\partial T_p}$ is the specific heat of electrons, hot phonons and the rest of the lattice respectively, f is the fraction of total modes that are strongly coupled with the electrons where as $(1-f)$ lattice modes that are more weakly coupled barely contributes to the temporal evolution of T_e and has been therefore neglected. The decay time τ_β describes anharminic decay of hot phonons. The solution for the three temperature model can be given by the double exponential formula, can be written this way

$$\theta(t)\left[K_1 e^{-t/\tau_1} + K_2 e^{-t/\tau_1}\right] \tag{3.36}$$

where τ_1 and τ_2 are the decay time of the two dynamics, $\theta(t)$ is a step function that accounts for the pump pulse incident on the sample, and K_1, K_1 are constant amplitudes.

3.3.3 Differential Reflectivity Model

Formulating differential reflectivity to fit the time-resolved experimental data is the corner stone for this thesis work. The model is based on the classical Drude-lorentz model to calculate total dielectric function of the system(see section3.1). We used the result of the static fit parameters reported in section 3.1.4.

To study the non-equilibrium dynamics in the Bi2212 optimally doped sample due to the pump pulse excitation in the variation of reflectivity we need to fit the $\Delta R/R$ data with a procedure. The differental signal can be represented by equation 3.37.

The differential signal is proportional to the change in electronic and lattice temperatures of the sample during the pump excitation. In classical Drude formalism the ω_p and γ_D are the only terms that depend on the temperature due to the pump excitaion. To fit the differential refletivity data we choose these two parameters of the Drude part that changes during the pump excitation.

$$\frac{\Delta R}{R_{eq}} = \frac{\left(R_{exc}\left[\omega_p^{'}, \gamma_D^{'}\right] - R_{eq}\left[\omega_p, \gamma_D\right]\right)}{R_{eq}} \tag{3.37}$$

Where ω_p and γ_D are the plasma frequency and scattering rate of Drude for the equilibrium reflectivity(i.e taken from the static fit) (see table 3.1) while the $\omega_p^{'}$ and $\gamma_D^{'}$ are the plasma frequency and scattering rate of Drude for the excited system by the pump pulse (1.5 eV).

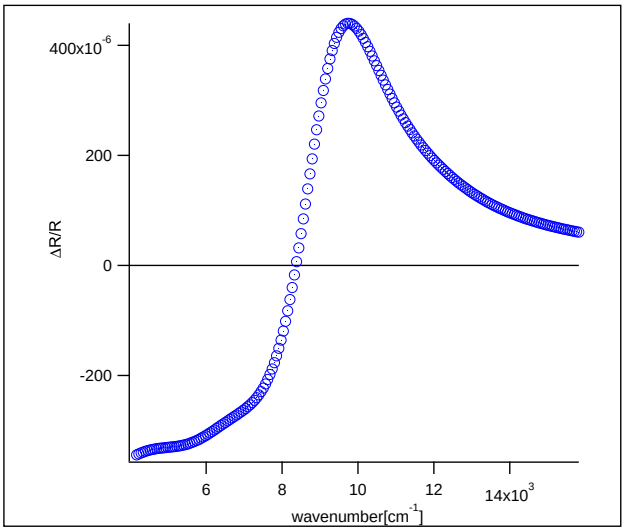


Figure 3.7: The differential reflectivity model calculated by changing only the ω_P and γ_D.

The temperature dependence of these parameters is key point to let them free inorder to take to account the temperature change of the sample due to the incident pump pulse. The γ_D has a character of changing the amplitude of the signal of the $\Delta R/R$ without changing the sign change point where as ω_P changes the sign change point with respect to what we have in γ_D and changes largely the low frequency part (see figure 3.9 and 3.8). so this behavior of the parameters are important to reproduce the exact sign change point. The black arrow in the figures shown in the direction of increasing temperature.

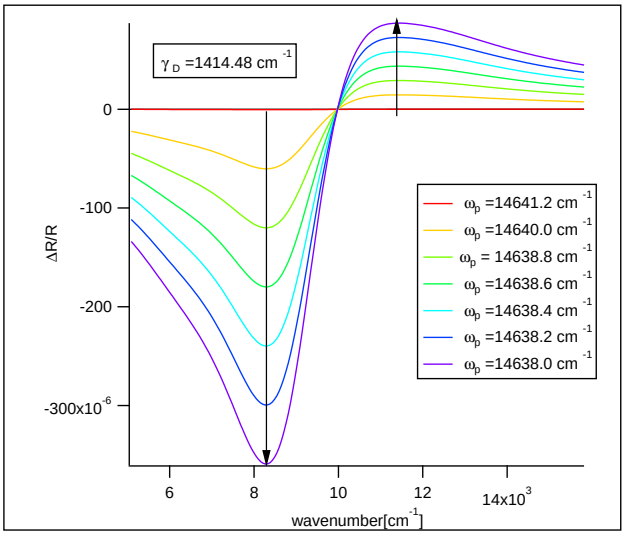


Figure 3.8: The differential model: the different plots shown are made by slight change of ω_P with respect to the equilibrium value. The black arrows show the plots are with decreasing ω_P.

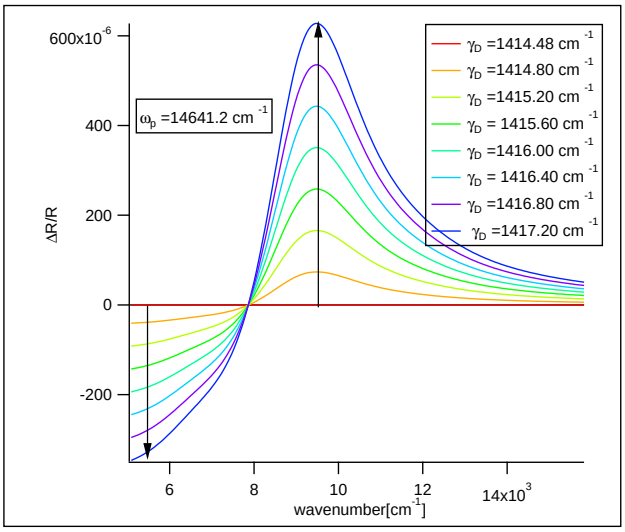


Figure 3.9: The differential model: the different plots shown are made by slight change of γ_D with respect to the equilibrium value. The black arrows show the plots are with increasing γ_D.

The procedure we prepare for the differential fit has a number of advantageous; it is easy and friendly to use by letting only two parameters vary but the others are fixed, less time consuming, it gives a good approximation in the MIR spectral region (see figure 3.7), it is implicitly Kramers-Kronig relation constrained, and finally suitable to describe temperature dependencies.

CHAPTER 4

Experimental Set-up

This chapter is devoted to the detailed description of the experimental setup schematized in figure 4.2 and 4.3. The chapter organized in the following way: in the first section is a brief description of the pump-probe technique. The second section is about the description of the generation, compression and amplification of ultrashort laser pulses at a repetition rate of 250 kHz [25, 26]. The third section is about the pulse characterization both in time and space while the last section is about the data acquisition system and the experimental improvement made using the SOLAR monochromator(i.e. M266).

4.1 Pump-probe technique

Pump-probe technique uses two beams (see figure 4.1); the strong beam called pump and the weak one called probe. A pump pulse excites the sample and takes it out of the equilibrium state. The pump beam passes though Scan delay this helps us to pump the sample at regular interval. The interval between two pumps should be longer than the response of the sample to ensure that there is no overlap of excitation events between the current pump and the previous pump. The second pulse probes the response of the system due to the excitation event created by the pump. To come up with a complete picture of the system response to the event we need to probe the sample over the entire cycle.

The way the delay line works is fairly simple. There is a retro-reflector on a rail system. The retro-reflector can be positioned along the rail by computer control of a stepper motor. If the retro-reflector moves backwards and lengthens the path, it takes that much longer for the pump pulse to reach the sample than the probe beam.

For example: If you moved the retro-reflector back 1 mm then the path is lengthened 2 mm which takes the beam $(2 \cdot 10^{-3}m) / (3.0 \cdot 10^{8}m/s) = 6.7$ picoseconds longer to reach the sample. This means you can probe the sample 6.7 picoseconds after it has been pumped. If you keep doing that you can probe it $0, 6.7, 13.4,$ e.t.c. picoseconds after it has been pumped. This gives us the time evolution of optical property of the system at one point on the surface of the sample as a function of time. This works when we have both the spatial and temporal coincidence between the two beams.

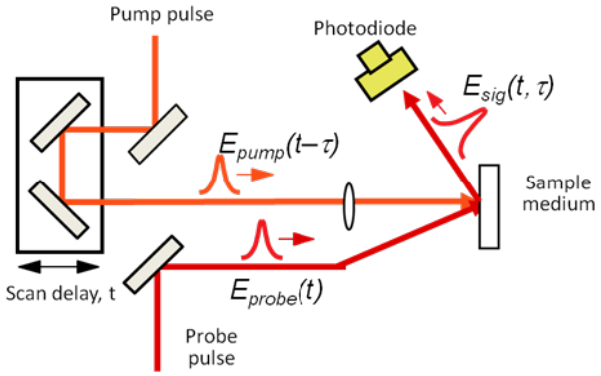


Figure 4.1: Typical schematic set-up of the pump-probe technique

4.2 Laser system

As shown in the figure 4.4 the laser source has five major components and the process to produce the short compressed pulse has six steps [27, 28, 29, 30].

1. The Verdi produces $18W$ of continuous wave laser light to pump the Mira-Seed $(8W)$ and RegA $(10W)$.

2. The Mira Seed produces laser pulses centered at 800 nm wavelength with $4nJ$ energy and $25 - 50$ nm bandwidth with a repetition rate of 76 MHz.

3. The stretcher rises the pulse duration of the ultrashort laser pulses up to 50 ps.

4. The stretched pulses goes to RegA 9000 are amplified up to 4, $30nm$ bandwidth at $250kHz$ repetition rate.

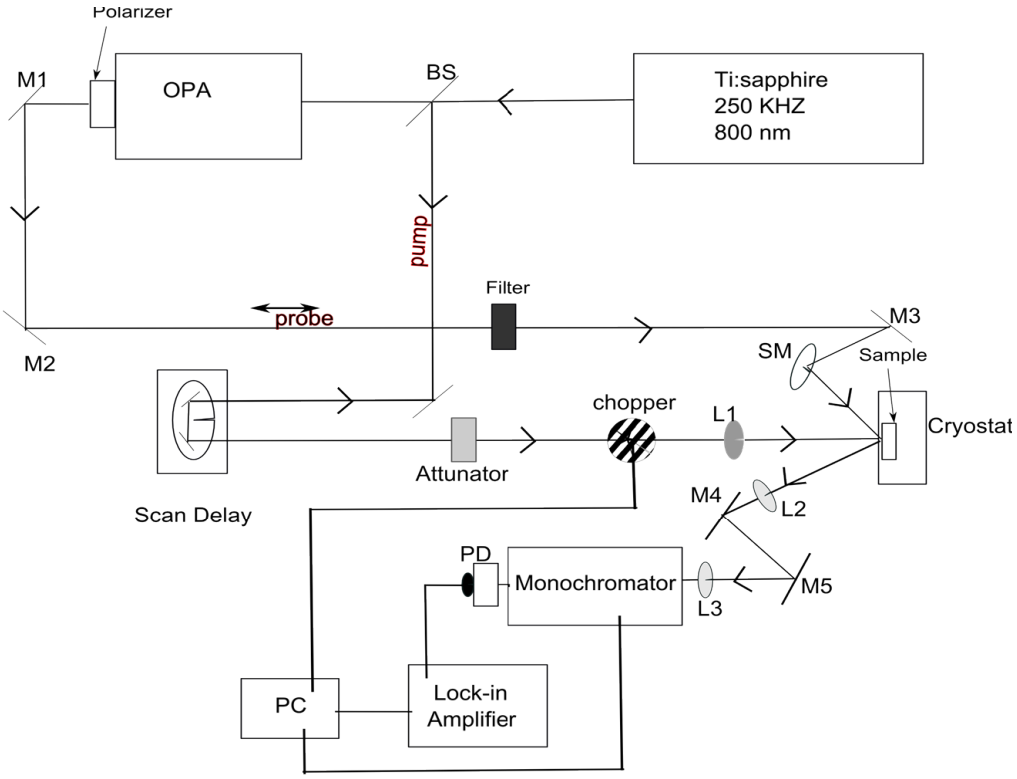


Figure 4.2: Where the box in the top right corner represents the laser system which produces the 800 nm laser with a 250 kHz repetition rate; BS= the beam splitter has 10/90 reflectivity to transmitivity ratio; OPA = optical parametric amplifier; M1, M2, and M3 are the gold mirrors used to direct the pulses to the sample where M4 and M5 are used to direct it on the photo diode; PD= photo diode; SM (f=30 cm)= spherical lens used to focus the probe on the sample; L1 (f= 40 cm) = lens used to focus the pump pulse on the sample; L2 (f = 12.5 mm) = used to collect the reflected probe from the sample. L3 (f=7.5 mm) = used to focus the reflected probe on the entrance slit of the M266 monochromator PC = the computed used to display the signal.

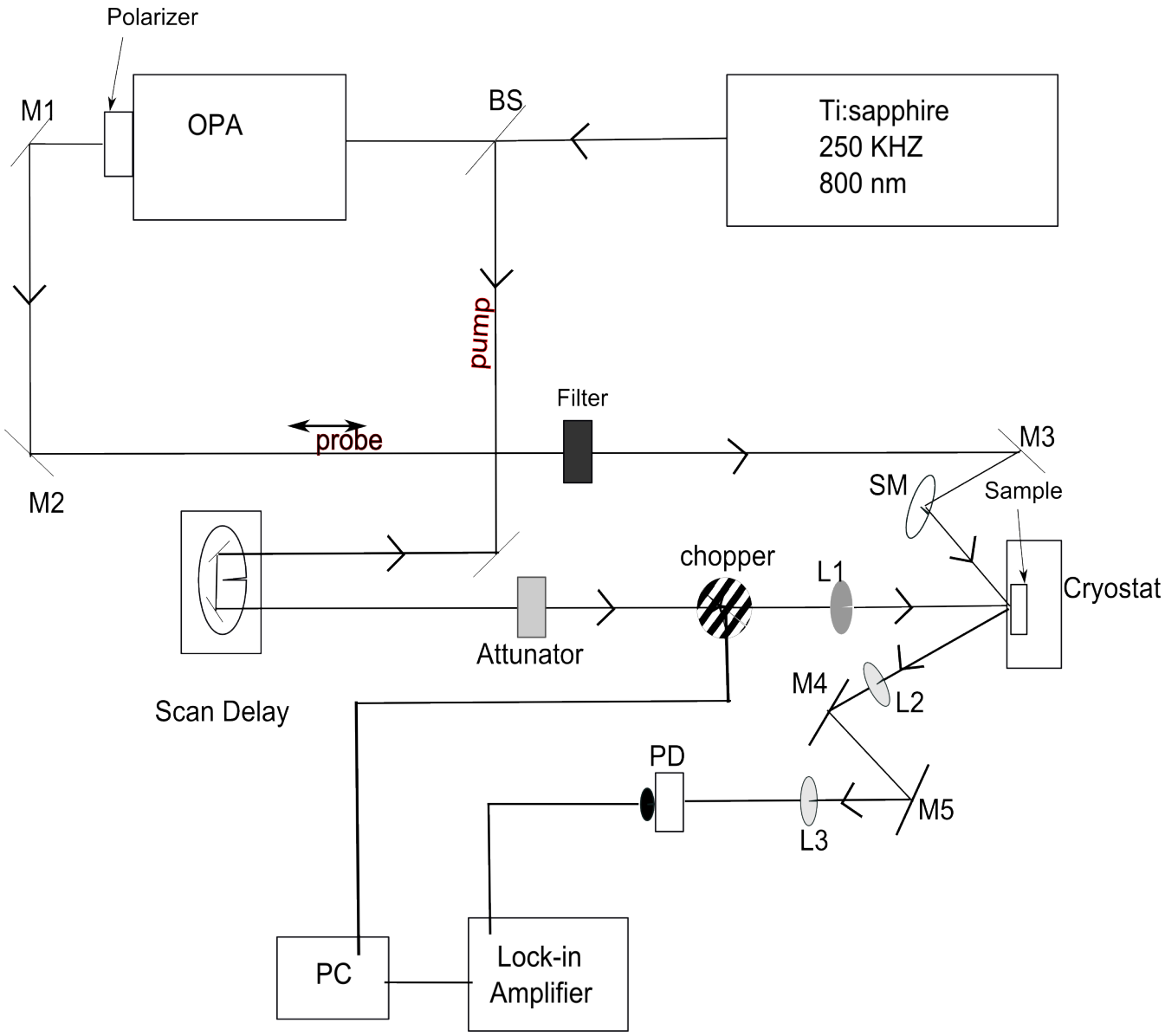


Figure 4.3: Optical set-up without the Monochromator. The only difference from figure 4.2 is that, this setup is with out the monochromator.

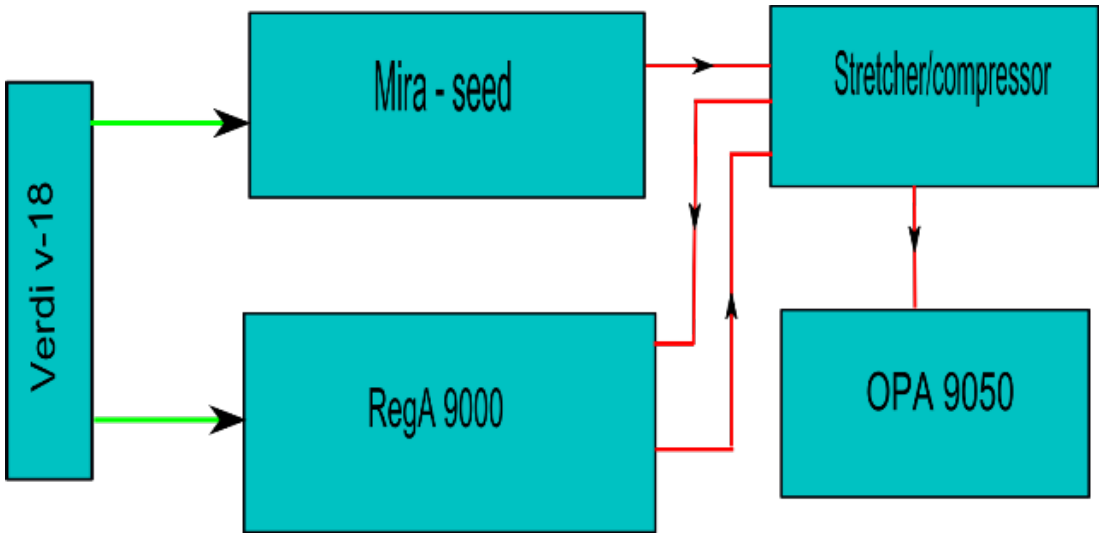


Figure 4.4: The Laser source

5. The amplified pulses are then send back to the strechter/compressor this time for compression in time down to $50fs$ pulse duration is 3.

6. The compressed pulses are splitted by a beam splitter (BS) the 10 reflected beam is used as a pump pulse for the experiment and the 90 transmitted beam is used as a source beam for the OPA 9050.

4.2.1 Optical pump(Verdi V-18)

In our laser system the Coherent Verdi V-18 is the optical pump for both the Mira Seed and the RegA. It is a compact solid-state diode-pumped, frequency doubled Nd:Vanadate (Nd:YVO4) laser that provides continuum monochromatic green (532 nm) output, with 18 W of power output.The laser head uses a Neodymium Vanadate (Nd:YVO4) crystal as active medium with the pump power provided by fiber delivery; this medium is a homogeneously broadened system, so the Verdi tends to naturally run single frequency, with the etalon reinforcing this behavior.The laser is frequency-doubled because its lasing wavelengths are 914 nm, 1064 nm and 1342 nm. Taking $c = \upsilon \cdot \lambda$ (speed of light [c] = wavelength [λ]$\cdot$ frequency [υ]) into account it is clear that doubling the frequency will halve the wavelength, bringing the middle lasing wavelength (1064 nm) into the green part of the spectrum (532 nm).Because of the very short lifetime of the upper-state excitations in Nd:Vanadate (Nd:YVO4)

3.2 several watts of the pump power is needed to reach the saturation level and consequently complete population inversion in the Vanadate.

4.2.2 Laser Oscillator(Mira-seed)

The laser oscillator or optical resonator see figure 4.5 is a femtosecond mode-locked Ti:Sa laser. In simple terms the oscillator allows a single short pulse of light to bounce back and forth between its mirrors. With the modes locked in phase a pulse can be formed for full description of the mode-locking process see 4.2.2.1. Each time when the pulse reaches the output coupler i.e. a partial mirror, a small percentage of is allowed to pass through to form the output of the laser.

The Mira seed Laser uses a Ti:Sa, i.e. Al_2O_3 doped with Ti_2O_3 as an active medium to convert the continuous wave pump laser from the Verdi V-18 in to short laser pulses centered at 800 nm with bandwidth ranging from 25-50 nm. These short pulses have repetition rate of 76 MHz and an average power of about 500 mW is produced.

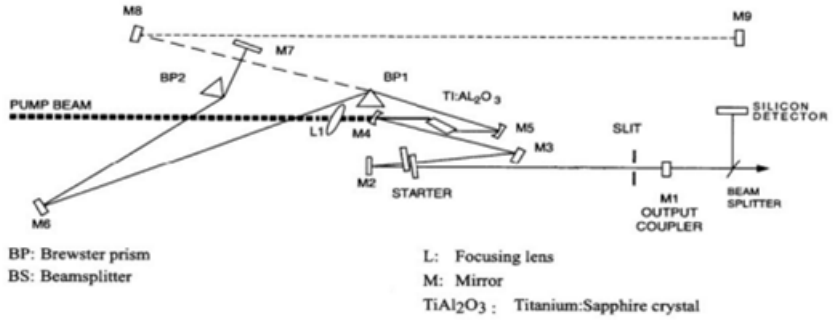


Figure 4.5: Mira seed oscillator

The Mira Seed oscillator uses a pair of prisms as shown in figure 4.6 to compensate the positively chirped dispersion of the ultrashort pulse. The choice of a material, orientation and distance between the prisms is such that they introduce a net negative GVD, canceling out the positive GVD due to travel inside the other optical media [31].

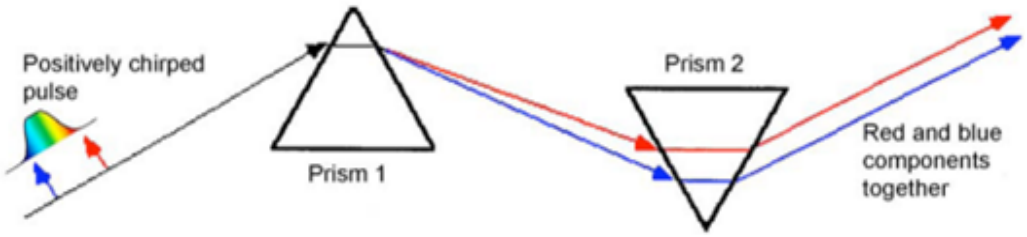


Figure 4.6: Group velocity dispersion compensation

4.2.2.1 Optical Kerr effect for Mode-locking in Mira-seed

The physical process behind the mode-locked Mira emission is the optical Kerr effect.The optical Kerr effect is a non-linear self-induced effect happens when an intense light is traveling through an active medium. The kerr effect can be described as a modification of the refractive index induced by the electric field of the e-m radiation itself. Scottish physicist John Kerr discovered its occurrence in 1875 and the effect can occur in glasses, crystals and gases, though certain materials display the effect stronger than others [31]. The intensity dependent refractive index (IRDI) in the material is given by the following formula

$$n\left(I\right) = n_0 + n_2 I \tag{4.1}$$

The above equation governs the optical Kerr effect where $n\left(I\right)$ is the total refractive index, n_0 is the linear refractive index, n_2 is the second-order nonlinear refractive index and I is the intensity of the incident light. Equation 4.1 highlights the fact that the light itself can alter the index of refraction. When the intensity of the light is high enough the electric field of the light becomes strong enough to distort the atoms of the material and change its refractive index. As the beam is more intense in the center than the edges, the index of refraction becomes higher in the center than at the edges, which causes the light to focus. The effect of focusing due to optical Kerr effects is known as Kerr lens or Self-focusing. The focusing due to the Kerr lens stops when the beam's diameter is narrow enough that its linear diffraction becomes stronger and compensates focusing (see Figure 4.7).

The Kerr lens is only formed when the intensity of the light is extremely high, such as the instantaneous intensity of a mode-locked pulse. The weak intensity of a

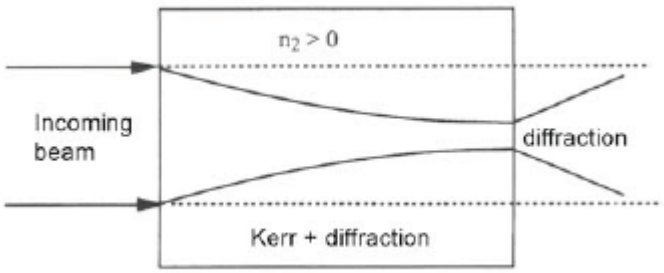


Figure 4.7: The self-focusing of a laser beam in a medium with n2 > 0

CW laser is not intense enough to induce an optical Kerr effect. This mechanism of self-focusing is used for mode-locking in the Mira-seed oscillator where the insertion of a slit or aperture in the laser cavity triggers the mode-locking. In fact the intense part of the pulse in the laser cavity are focused much more strongly than the weak tails which are almost not focused. The inner and intense part of the laser have now a transverse structure reduced in size and less vulnerable to losses in the cavity, while its weak and outer one experiences enhanced losses. This leads to self mode-locking of the laser. The slit as it shown in figure 4.8, increases the difference between the losses experienced by the weak part in respect to the heavily attenuated part. The diameter, position and shape of the slit must be calculated and adjusted precisely.

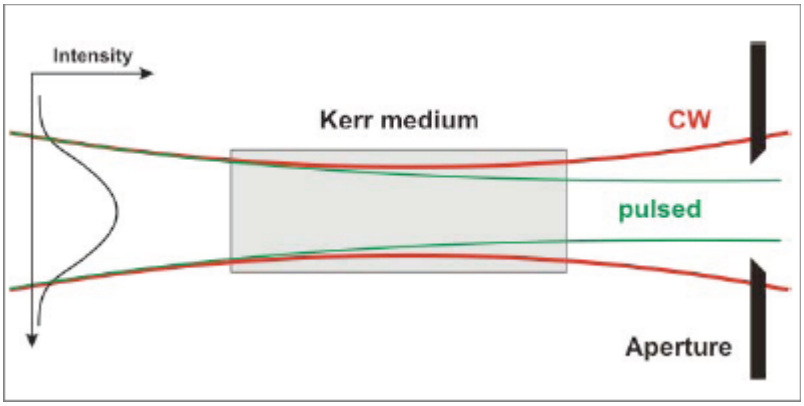


Figure 4.8: Kerr lens mode-locking

4.2.3 Stretching and Compression Stage(Compressor/stretcher)

The stretcher is used to increase the Mira-seed pulse duration up to 30 ps, while the the compressor should reduce it back to about 50 fs after amplification. The most ef-

fective way to achieve this purpose is with grating-based stretcher and compressor(see figure 4.9). In the following we discuss each step separately.

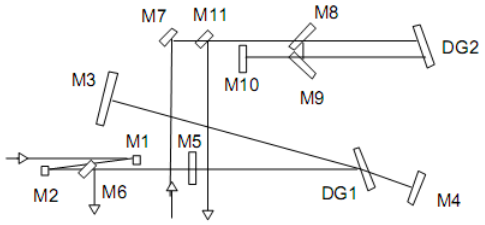


Figure 4.9: Expander-Compressor layout

Figure 4.10 shows the simplest grating configuration, where long-wavelength components travel a larger distance than the short-wavelength components.This introduces an effective negative dispersion i.e. opposite to the one exprienced by the same pulse in the dispersive medium. The dispersion can be tuned easily by changing the distance between the two gratings. This setup is used as a compressor. Figure 4.11

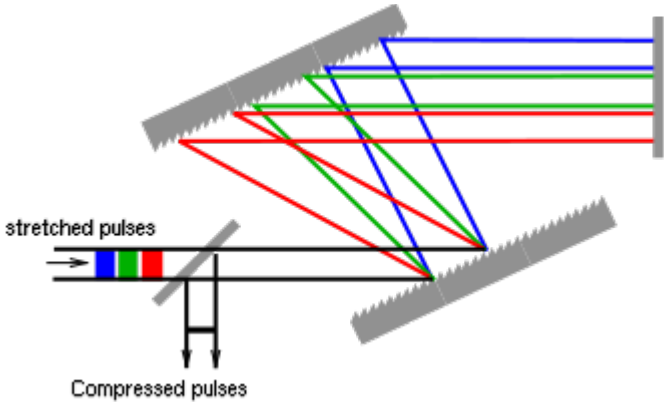


Figure 4.10: Schematic layout of a grating-based compressor. where the long-wavelength shown in red and the short-wavelength shown in blue.

shows the grating-based stretcher which involves also two focusing lenses that act as a telescope. The lenses are placed at a distance 2f (where f is the focal length of the lens) from each other and at a distance L from the gratings. If $L < f$, the setup acts as a positive-dispersion stretcher and if $L > f$, it is a negative-dispersion stretcher. In our case we have a positive disperion stretcher.

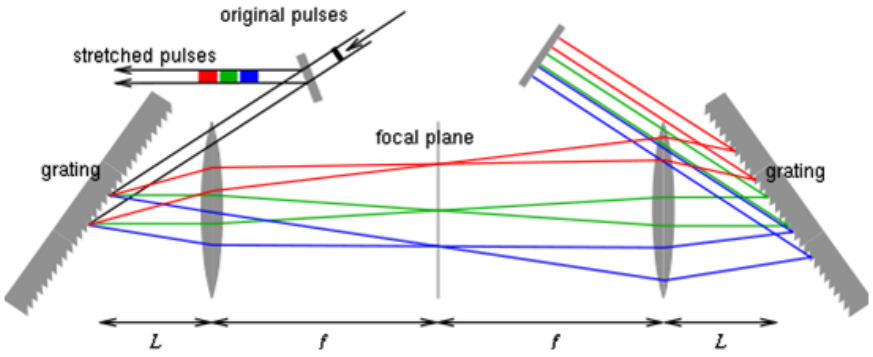


Figure 4.11: Schematic layout of a grating-based stretcher.

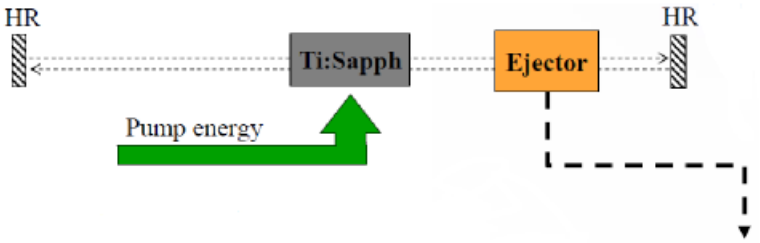


Figure 4.12: RegA Q-switch operation

4.2.4 The Laser amplification(RegA)

RegA 9050 is a regenerative amplifier system which amplifies the pulse energy from the Mira Seed. RegA requires only a few mW of output power from the oscillator and amplifies it to the μJ level [30]. The verdi laser is used as a pump source for the RegA, amplification of the Mira-seed oscillator occurs at a repetition rate of 250 kHz.

The RegA 9050 can operate in two ways the first one is when the Verdi pump beam induces gain to build up in the Ti:Sa, the regenerative amplifier is working in CW when the ejector is off and as soon as the ejector is turned on a pulse is ejected. In this case the RegA 9050 acts as the stand alone laser cavity, it can work in CW or Q-Switched (see figure:4.12.

The regenerative amplifier can also be used as an amplifier for seed pulses. The injector traps the seed pulse in the cavity, while the pump beam makes gain to establish in the active medium. The pulses are amplified at each pass through the Ti:Sa (so at each round trip in the cavity) and finally the ejector allows the pulse to

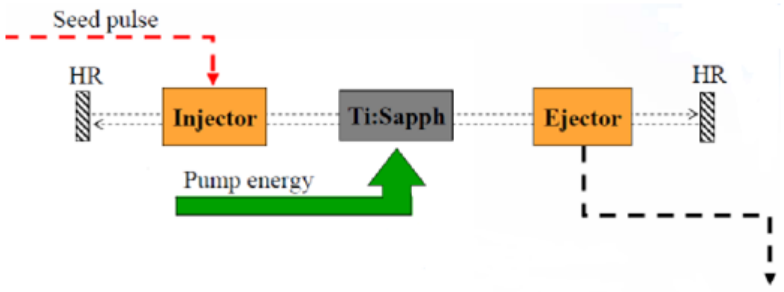


Figure 4.13: The schematic view of the RegA seeded operation. Taken from [3]

exit the cavity (see figure 4.13, 4.14).

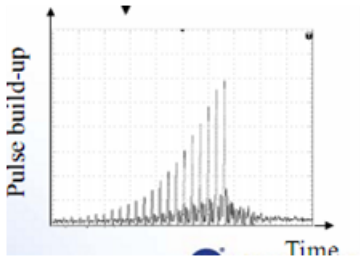


Figure 4.14: The pulse build up in the RegA seeded operation

The pulse ejection and injection in RegA are performed by an acusto-optic modulator (AOM) that works with high efficiency and so fast that manages to exploit the 3 -long energy storage time of the Ti:Sa to produce stable operation at very high repetition rate.

The RegA amplification layout consists of Titanium: sapphire modelocked oscillator, Titanium: sapphire regenerative amplifier(RegA 9050), and Verdi pump laser. The RegA amplifies the low energy femtosecond pulses from the Mira laser to of energy as it described above.

4.2.5 The Optical parametric Amplification (OPA)

An optical parametric amplifier (OPA) is one example of this more general class of nonlinear optical devices. In optical parametric amplification, the shortest wavelength beam is called the pump and has the most power. The other input beam is called the signal and the resulting third beam is called the idler. Under proper conditions, the conversion process can coherently accumulate through the complete passage through

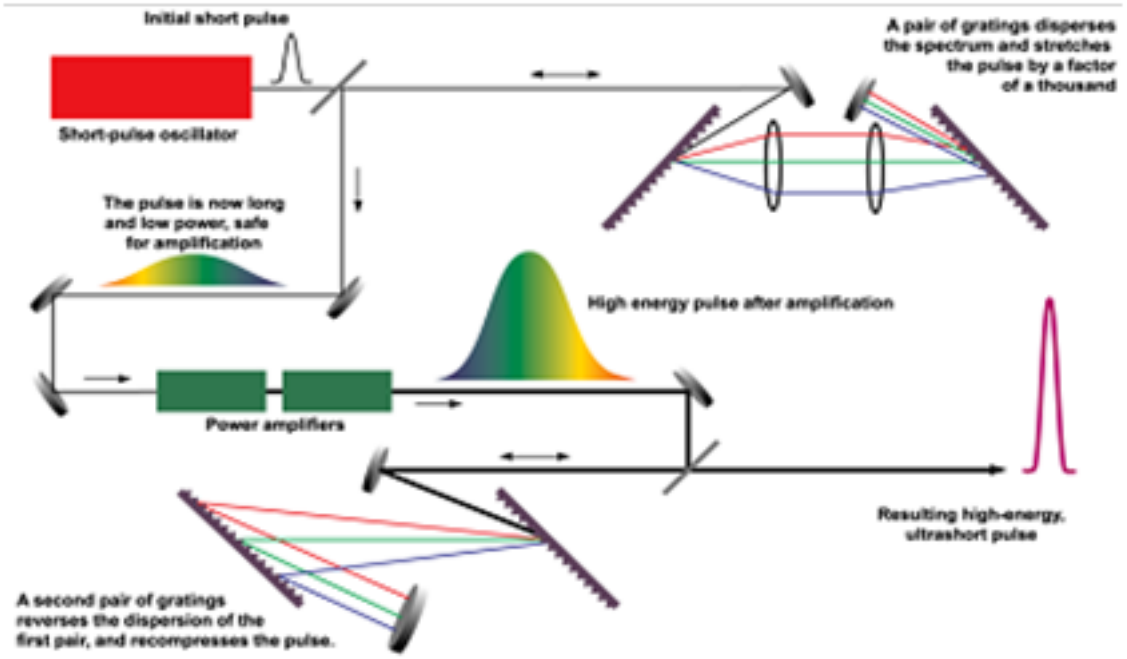


Figure 4.15: The RegA amplification layout

the nonlinear material and the signal and idler waves both grow with the pump wave decaying [25]. The energy conservation condition is expressed as:

$$\omega_{pump} = \omega_{signal} + \omega_{idler} \tag{4.2}$$

For a given pump wavelength, the matching between the two input beams is given by rotating the direction of propagation through a birefringent OPA crystal. By rotating the crystal through just a few degrees the signal wavelength can be tuned from 1200 nm to 1600 nm and the idler simultaneously scans from 1600 nm to 2400 nm. For a given signal wavelength and the idler wavelength can be drived from equation 4.2

$$\lambda_{idler} = \frac{800nm \cdot \lambda_{signal}}{\lambda_{signal} - 800nm} \tag{4.3}$$

where λ_{idler} is the wavelength of the idler, 800 nm is the wavelegngth of the pump, and λ_{signal} is the wavelgth of the signal.

The OPA 9850 is a wavelength conversion accessory for the Coherent RegA Titanium: sapphire mode-locked regenerative amplifier system. To generate ultrashort laser pulses tunable in wavelength with an amplified Ti: sapphire laser system, one needs to use an optical parametric amplifier (OPA). The Optical Parametric Amplifier used in thse thesis has produces amplified femtosecond pulses tunable from 1200

to 2400 nm at a 250-kHz repetition rate [29]. As can be seen in the figure 4.16 the

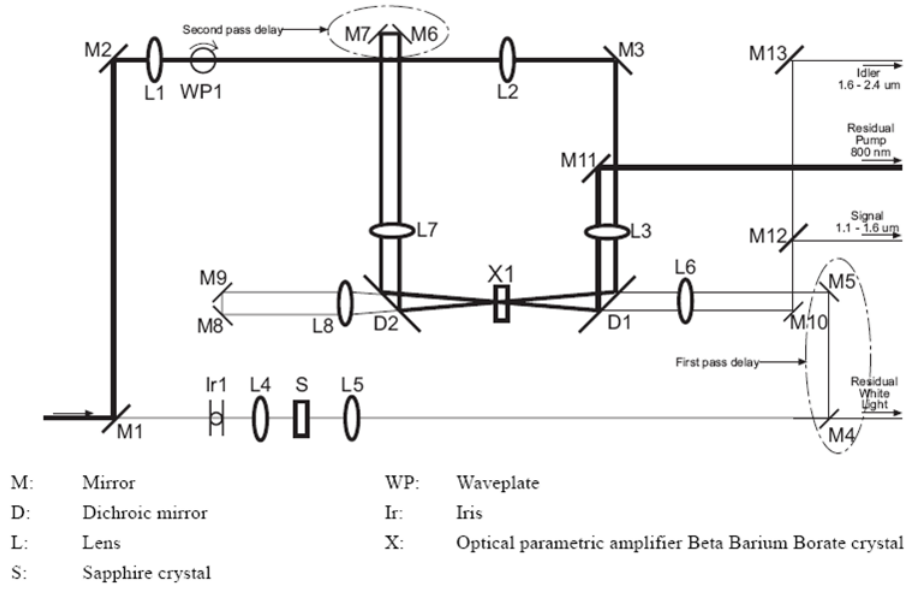


Figure 4.16: The layout of the OPA

800 nm RegA output enters the OPA and is split by M1 with 75% of the energy going into the OPA crystal (X1) via M2, passing through a wave plate (WP1), and from M3 to D1. The remaining 25% passes through an Ir1, and is focused by lens L4 onto Sapphire crystal "S", which produces a white light in the 460-1600 nm spectral range. The white light (WL) is collimated by lens L5. The WL then passes through an adjustable optical delay (first pass), consisting of M4 and M5. M4 and M5 share a common mount that is adjusted by an external micrometer so that the optical paths of the WL and 800 nm at optic D1 exactly match. The 75% of the incoming RegA beam is combined with white light which come from a first pass through the OPA crystal. After the first pass through the OPA crystal (BBO material), a small amount of signal and idler are generated. The signal is then separated from the 800 nm pump and is reflected off of a second fixed optical delay, mirrors. The 800 nm pump is reflected off of an adjustable optical delay, mirrors. The 800 nm pump and signal beam are then recombined for a second pass through the OPA crystal. After the second pass through the OPA crystal, the idler, signal, and remnant pump beams exit the OPA. The signal wavelength can be angle-tuned by an external micrometer. The crystal angle allows the selection of one wavelength out of the continuum and

then amplifies the signal strongly at that wavelength.

4.3 Characheterization of pulses

A full characterization is needed to correctly determine the experimental conditions.The parameters to be characterized are the fluence on the sample, the pulse duration and thier spectrum.These parameters can be characterized with the following procedures:

1. The pulse duration can be measured with an autocorrelator and Optical sampling techniques (i.e. cross-correlation measurements). The cross-correlation measurements is possible only when a shorter reference pulse is available.

2. The peak power can be measured directly with a power meter.

3. The pulse energy can be calculated from the average power and repetition rate.

$$E_{pulse} = \frac{P_{avg}}{Rep.rate} \tag{4.4}$$

where E_{pulse} is the pulse energy, P_{avg} is the average power measured directly using the photo diode, and Rep.rate is repetition rate. From the pulse energy the fluence can be calculated as

$$Fluence = \frac{E_{pulse}}{A} \tag{4.5}$$

where $A = \pi r^2$ is the area of the spot. The pump fluence before the attuenator can be calculated as

$$I_{max} = \frac{P_{max}}{Rep.rate \cdot \tau_{pulse} \cdot A} \tag{4.6}$$

where I_{max} is the maximum fleunce of the pump before the attuenator, P_{max} is the maximum power of pump measured using the power meter, $Rep.rate = 250$ kHz is the repition rate of the pump, τ_{pulse} is the pulse duration of the pump and A is the spot of the pump on the sample. Considering the effects of the two plates in the attuenator and the windows of the cryostat we calculate the absorbed fleunce by the sample

$$I_{absorbed} = I_{max} \cdot 0.92 \cdot 0.92 \cdot 0.96 \tag{4.7}$$

The attuenator is used to set the pump fleunce at different values. The 0.92 is taking to account the the plates in the attuenator and 0.96 is to take in to account the window of the sample.

4. The spatial beam profiles can be measured by the CCD camera and an optical objective.

5. The probe spectrum can be aquired with a spectrometer (HAMAMATSU C9914GB).

4.3.1 Autocorrelation measurements

The measurement of the pulse duration of ultrashort laser pulses with ordinary electronics is impossible directly. One technique to measure the ultrashort laser pulse intensity versus time is the intensity autocorrelation. As it shown in the figure 4.17 this technique is based on the second harmonic generation (SHG).

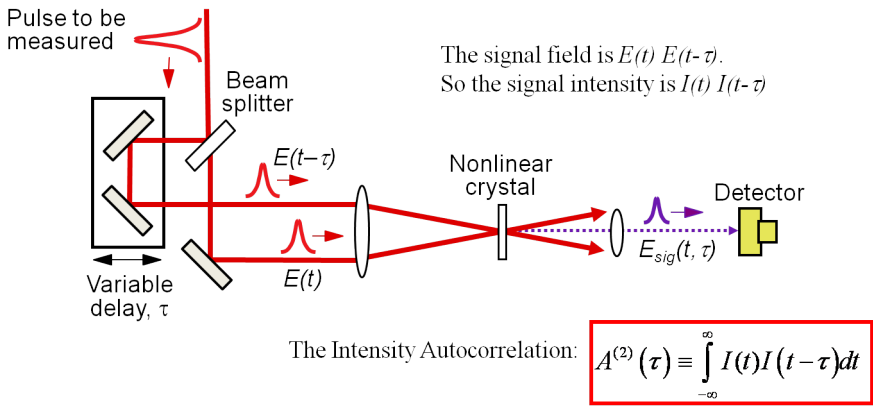


Figure 4.17: Internal look of the autocorrelator.

The pulse to be measured enter in the hole and splitted by a beam splitter; half of the pulse pass though a variable delay and both focused by a spherical lens on the second harmonic generator crystal. When the two identical pulses become coincident spatially and temporally the second harmonic signal is generated and the detector can measure the signal intensity versus the delay time. The signal prduced by the second harmonic has twice the frequency of the input pulse with a field envelope that is given by

$$E_{signal}^{SHG} \propto E(t)\, E(t-\tau) \tag{4.8}$$

where τ is the delay. The instantaneous intensity is proportional to the product of the intensities of the two pulses. And given by the formula

$$I_{signal}^{SHG} \propto I(t)\, I(t-\tau) \tag{4.9}$$

The photodoide is slow to resolve the instantaneous intensity, so it measure the integrated value:

$$A^2(\tau) = \int_{-\infty}^{\infty} I(t)\, I(t-\tau)\, dt \tag{4.10}$$

Where A^2 is the intensity autocorrelation. The superscript(2) implies the second-order harmonic autocorrelation. To calculate the bandwidth we have to consider the signal is the convolution of the two Gaussian pulses. So we have to divide it by $\sqrt{2}$ in order to get the deconvoluted pulse duration. For example the pulse duration of RegA output pulse is $50fs$ (see figure 4.18). All autocorrelation measurements should be totally symmetric; any lack of the symmetry is an indication of a lack of dispersion balance between the two beams of the autocorrelator or detector saturation.

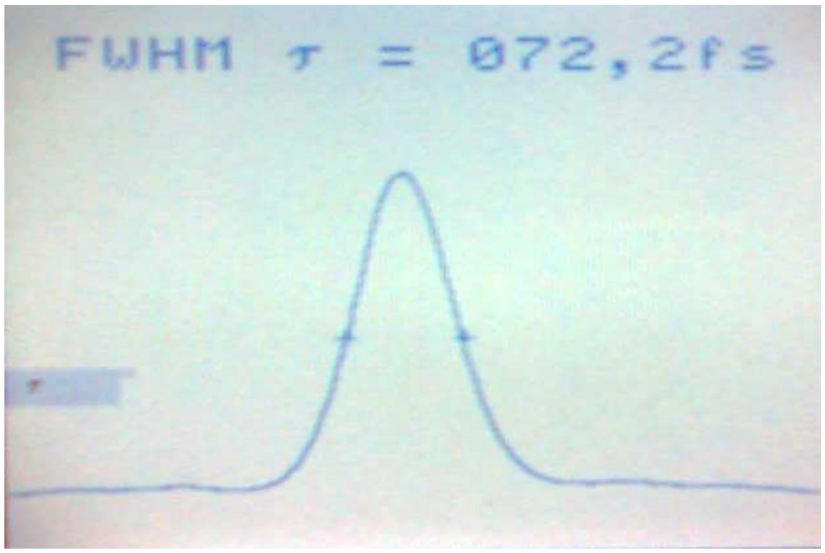


Figure 4.18: Shows the figure taken form autocorrelator of 800 nm pulse duration

4.3.2 Cross-correlation measurements

In order to determine the pulse duration of the OPA pulse (probe), we do a cross-correlation measurements. The experimental set-up we used for the cross-correlation measurement is shown in figure 4.2 except we used a second harmonic crystal(BBO

non-linear crystal) instead of the samples in the cryostat. After the crystal we put the photo diode that will measure the signal intensity versus the delay. Based on the assumption of the pump pulse doesn't pass through any medium up to the same position of the Autocorrelator or the pump pulse pass through a medium but it is compensated by the negative GVD created in the compressor. Having said that we do the measurements and we got the results shown in figure 4.19.

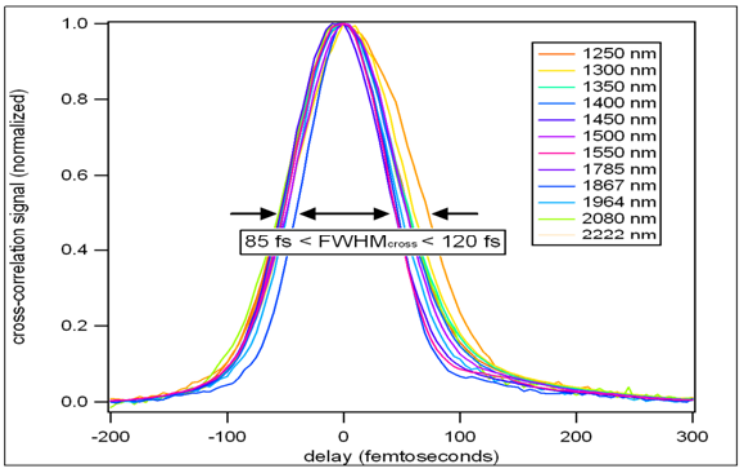


Figure 4.19: Cross-correlation measurements on the different wavelength of the probe pulse

$$FWHM_{OPA} = \sqrt{(FWHM_{cross})^2 - (FWHM_{800nm})^2} \tag{4.11}$$

where $FWHM_{OPA}$, $FWHM_{cross}$, and $FWHM_{800nm}$ are the full width half maximum of the OPA pulse, the cross-correlation and the pump pulse(800 nm) respectively. From autocorrelation measurements we have $FWHM_{800nm}$= 50 fs and From the cross-corelation measurments $FWHM_{cross}$ = 85 - 120 fs. Using equation 4.11 the $FWHM_{OPA}$ becomes $68.74fs - 109.09fs$ for the wavelength range $1200 - 2222nm$. This result is plotted in figure 4.20.

4.3.3 Peak Power of OPA

The power which is coming out of the OPA contains the Signal and the Idler, these two are orthogonally polarized. At an angle of the polarizer 220 ° we can get only

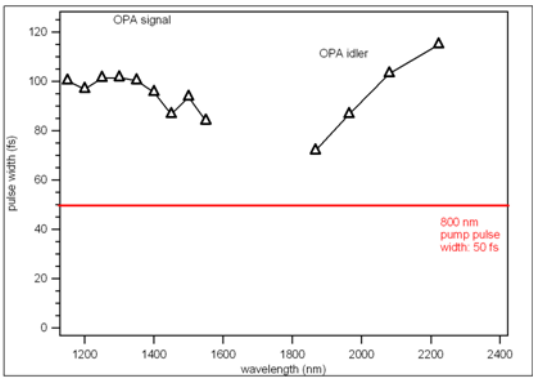


Figure 4.20: The pulse width from cross-correlation measurements versus the wavelength of the probe beam. Where the horizontal red line shows the pulse width of the 800 nm.

the Signal and at 130° only the idler. Using the circular polarizer the power of the signal and the idler can be measured separetly using the powermeter (see figure 4.21)

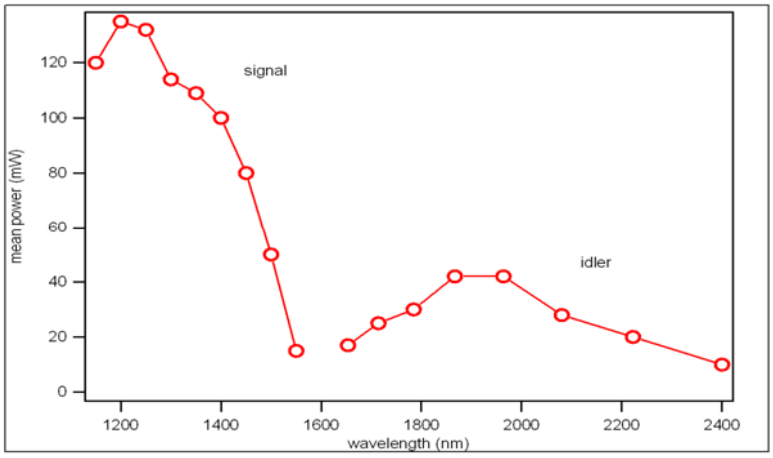


Figure 4.21: The signal and the idler power of the OPA versus the wavelength

4.3.4 Spatial beam profiles

The characterization of Spatial beam profile both the pump and the probe pulse size is important. Before we start any measurements we have to check the pump spot ($90\mu m$) is bigger in size than the probe spot ($37\mu m$). This is just because to make sure that we are probing the uniform and homogeneous part of the sample that is excited by the pump pulse (see figure 4.22).

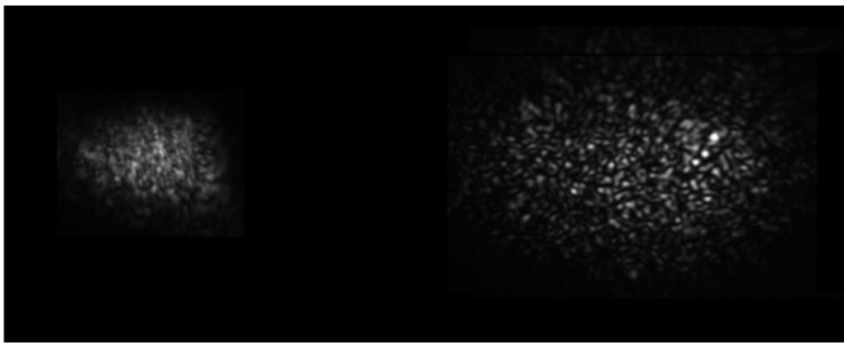


Figure 4.22: Shows the spot size of the pump and probe beam. Where the left side is the probe while the right side is called the pump.

4.4 Data Acquisition System and Main Improvements

In this experiment we use a new acquisition system by implanting the M266 monochromator before the photodiode. The monochromator is used to cut the broad probe signal in the form of the spectral lines with a bandwidth about 10 nm and scan in the range that the signal exists.

4.4.1 Experimental setup using the Monochromator

The use of M266 monochromator is to produce a single spectral line by selecting from a broadband signal input. The M266 monochromator works in the spectral range of 180- 3600 nm. It has an adjustable entrance and two exit(Lateral and axial ports) slit, three gratings, and two collimating mirrors. M266 monochromator is controlled automatically by interfacing with the computer using a High-speed USB (see figure 4.23).

The purpose of the two slits in this monochromator is to control the size and position of the beam passing through the slit. The edges of the slit are very carefully machined so that the distance between the two edges through which the light passes are equidistant all along the slit opening. The slit width (0-2000 micrometer) is adjustable, and controlled by the program. To focalise signal on the entrance slit we use a spherical lense.

Once signal enters from the entrance slit, it is redirected by the first mirror toward

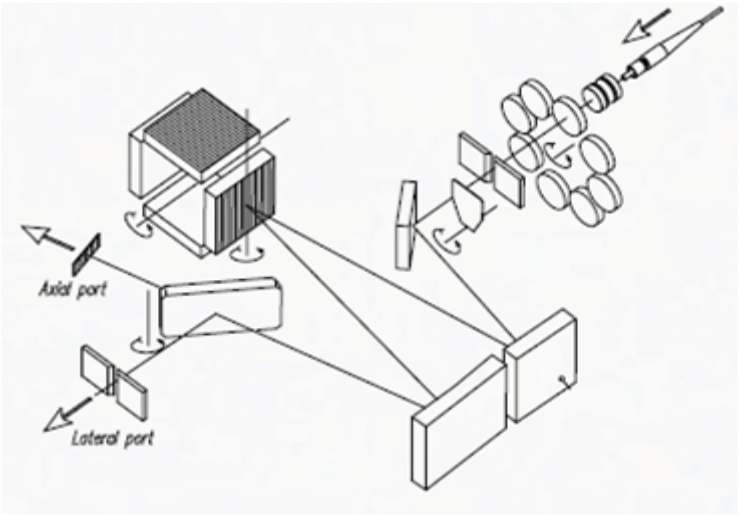


Figure 4.23: Exact M266 monochromator from solar laser systems.

the grating. The surface of these mirrors must be reflective in the wavelength region of the light involved. The surface can be polished aluminum, silver or gold. This metal is sometimes covered with a protective coating that prevents the metal from tarnishing, obviously also transparent to the light involved.

The grating (50x50x10mm) is used to disperse the wavelengths in space so that they are no longer parallel but instead leave the grating at slightly different angles i.e. angles dependent upon the wavelength. It is automatically controlled and we have three gratings each works in a specific wavelength range.

4.4.2 Characterization of the Monochromator

In the experimental set-up (see figure 4.2) we put Monochromator after the cryostat to can cut the broadband OPA signal in narrow wavelength band ($\approx 10nm$) (see figure 4.24. This method allows us to get a details information of the differential reflectivity around the sign change point (see section 5.3).

Putting the monochromator before the cryostat disperses the probe beam and it was difficult to focus on the sample with a small spot size.

We carryout also a measurment with interference Filters to check if we can able to select the a narrow wavelength band. The interference filter we used selects a narroe frequency band centred at 1320 nm with bandwidth of 12 nm (see figure 4.25).

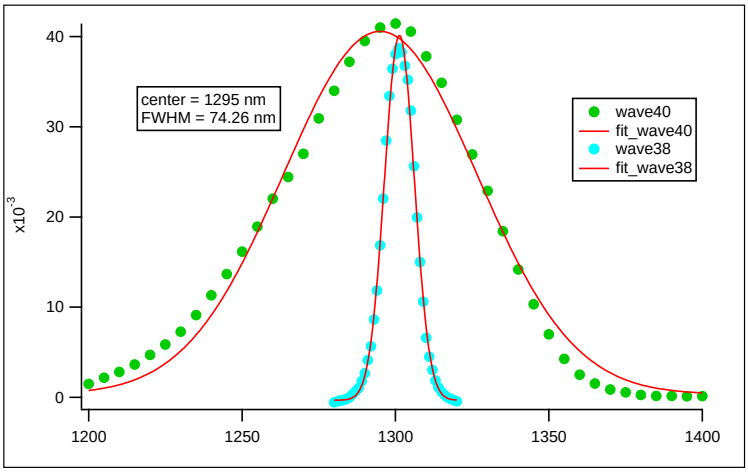


Figure 4.24: The Monochromatized signal ploted with the broad OPA pulse

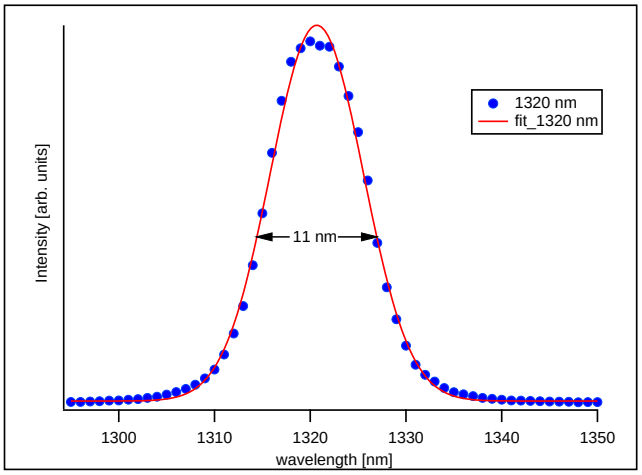


Figure 4.25: Measurement of the OPA signal in the narrow band by putting intefer-ence filter infront of the entrance slit

Another interesting check on the Acquisition system is whether we don't lose any resolution due to the monochromator acquisition system. From the cross-correlation measurements the pulse duration value of the OPA (i.e. the probe pulse) which is ≈ 70 fs. From the time-frequency indeterminacy principle.

$$\Delta\omega.\Delta t \geq \frac{1}{2} \tag{4.12}$$

and

$$\Delta\omega = \frac{2\pi c}{\lambda^2}\Delta\lambda \tag{4.13}$$

The maximum resolution in wavelength of the monochromator that we measure using the interference filter at λ=1300 nm, $\Delta\lambda$=12 nm (see figure 4.25) using these values the $\Delta\omega$

$$\Delta t \geq \frac{1}{2.\Delta\omega} = 45fs \tag{4.14}$$

Since the pulse duration from the indeterminacy principle is smaller than the cross-correlation measurements. We can conclude that we don't lose resolution with the monochromator acquisition system.

4.4.3 Lock-in detection

The Lock-in amplifier from Stanford research SR830m relays on the concept of phase sensitive detection for the operation. The main reason for using the a lock-in amplifier is to recover signals from noise. The phase sensitive detection refers to the modulation or rectification of an AC signal by a circuit which is controlled by a reference waveform derived from the device that modulates the signal[32]. The phase sensitive detector effectively responds to signals which are coherent (same frequency and phase) with the reference waveform and rejects all others. The problem of an AC signal is the average value is zero so to record a value from this kind of signal we must rectify it. We use a lock-in amplifer to exploit the frequency selection and the optimization of the signal-to-noise ratio 4.26. As can be shown in the figure 4.26 all the spectral noise not centered at ω remains AC modulated and is removed by a low-pass filter [33]. The photo diode detector multiplies two signals: the signalaquired from the experimental and the sinusoid signal generated from the chopper with frequency

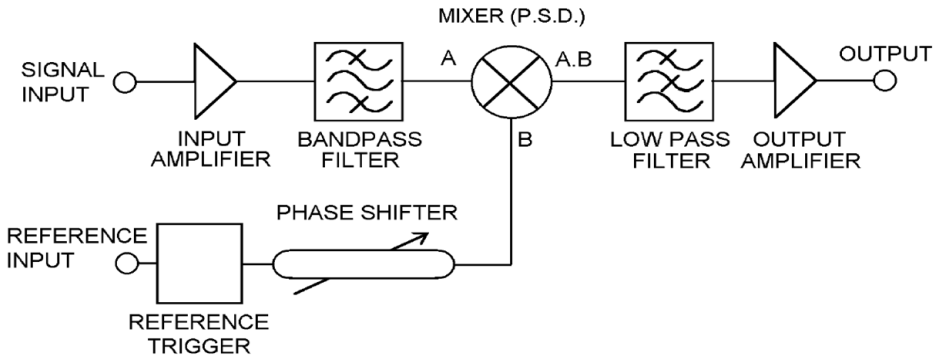


Figure 4.26: The Lock-in Detection system

equal to ($f = 13kHz$). The output signal from the photodiode is a product of input signal (experimental AC signal) and the reference AC signal. Let's now assume the inputs AC signal as $V_{input} = V_0 \cos(\omega_{in} t + \theta_{in})$ and similarly the reference AC signal $V_{ref} = V_1 \cos(\omega_{ref} t + \theta_{ref})$.

The photodiode detector output is given by the product of the two AC signals.

$$\begin{aligned} V_{PD} &= V_0 V_1 \cos(\omega_{in} t + \theta_{in}) \cos(\omega_{ref} t + \theta_{ref}) \\ &= \frac{1}{2} \left[\cos\left[(\omega_{in} + \omega_{ref})\, t + (\theta_{in} + \theta_{ref})\right] + \cos\left[(\omega_{in} - \omega_{ref})\, t + (\theta_{in} - \theta_{ref})\right]\right] \end{aligned}$$

All the spectral noise not centered at ω_{ref} remains AC modulated and it is removed by a low-pass filter. As we describe above the only signal that survive is when the frequency of the experimental AC signal is equal to the reference frequency i.e. $\omega_{in} = \omega_{ref}$.

$$V_{PD} = \frac{1}{2} V_0 V_1 \cos(\theta_{in} - \theta_{ref}) \tag{4.15}$$

Equation 4.15 shows that the output signal is a DC signal. So we conclude that the frequency of the lock-in reference frequency should be the same as the signal frequency (i.e. $\omega_{in} = \omega_{ref}$) then returning the noise-free DC component as the output of the lock-in amplifier.

This procedure allows us to acquire the pump induced $\Delta R/R$, without the noise related to other frequencies. The choice of the chopper's frequency has some constraints: it has to be the highest possible value, in order to suppress the $1/f$ noise, but lower than the laser repetition rate because, in that case, only a few pulses would pass through the open window of the chopper.

CHAPTER 5

Experimental Results

In this thesis work we performed time-resolved refectivity measurement on optimally-doped $Bi_2Sr_2Ca_{0.92}Y_{0.08}Cu_2O_{8+\delta}$ single crystal (T_c= 94 K). The sample was kept at room temperature in ultrahigh vacuum (10^{-8} mbar). The tunability of the laser source repetition rate allows us to avoid significant average heating of the sample and to optimize the signal-to-noise ratio in the detection of the transient reflectivity variation. A repetition rate of 250 kHz is used through out this thesis work.

We aquired two different sets of data: the first with the full bandwidth of the OPA in the spectral range of 1200-2400 nm (with 50 nm step) by exploiting the Optical parametric amplifier(see section 4.2.5) and the second one is using the monochromator to improve the spectral resolution (see section 5.3).

5.1 Tuneable wavelength pump-probe experiment

In the pump-probe technique we are measuring the modifications of the optical properties of the sample.

The figures 5.1 and 5.3 are the 2D matrix plot of the pump-probe experiment in the full spectral range where the color scale is $\Delta R/R$, the x-axis is the delay time in picosecond and the y-axis is the wavenumber. Figures 5.2 and 5.4 are $\Delta R/R$ versus the delay time of single scan measurements for each wavelength, where a sharp increase of $|\Delta R/R|$ occurs at zero delay due to the incident pump pulse.

The measurement of the full spectral range were performed at absorbed pump fluence (ϕ $\sim$892 and 446 $\mu J/cm^2$) for a total scan range of 20 ps. The absorbed pump fluence calculation is explained in section 4.3. Each measurement is resulted by averaging out large number of scans(approximately 300 scans for each wavelength).

The number of scans increase when the the absorbed pump fluence decreases in order to maximize the signal to noise ratio.

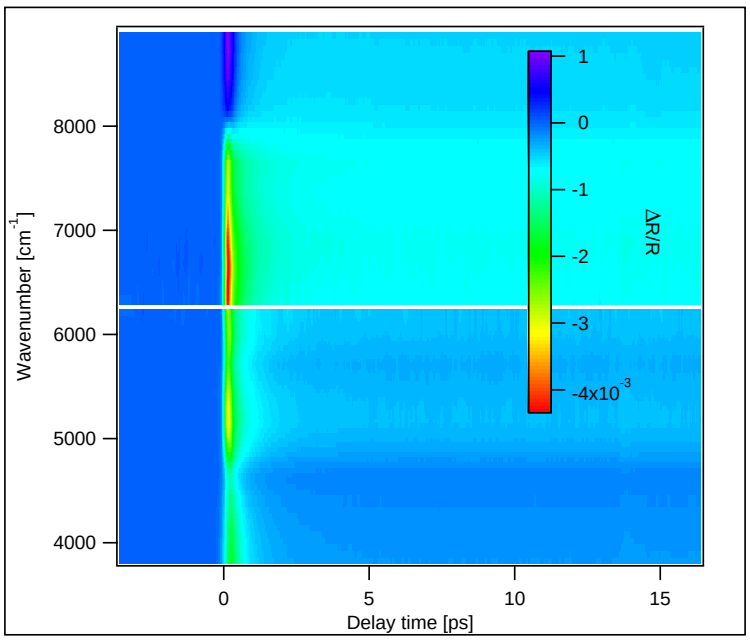


Figure 5.1: The graph is 2D matrix plot at $\phi \sim 892\ /cm^2$ in spectral range of 4166.67 - 9174.31 cm^{-1}. A horizontal white line present in the plot is due to the OPA laser source gives too low signal in that spectral range.

In the 2D matrix plot we can clearly see the sign change point in the reflectivity from positive (blue) to negative(red) at about 8000 cm^{-1}. The sign change point is slightly different for different pump fluence (we discuss this in section 5.5). Different dynamics in the vicinity of the sign change point is obseved (see inset of 5.2) this is because of the dynamics of sign change. This finding demonstrate that the common approach of treating single wavelength $\Delta R/R$ traces in terms of a simple 2/3 temperature model is wrong in the vicinity of the sign change.

However only far enough from sign change point the dynamics of the scan at a single wavelength can be interpreted in the usual approach of the 2/3 temperature model. We fit the data in order to give an estimation of the relaxation dynamics duration far from the sign change point. And we report figure 5.5 the fit of single scan measurement. The fit is done with double exponential function for the two dynamics contribute to the signal(see equation 6.1). We find τ_1= 103.43 fs and τ_2 =

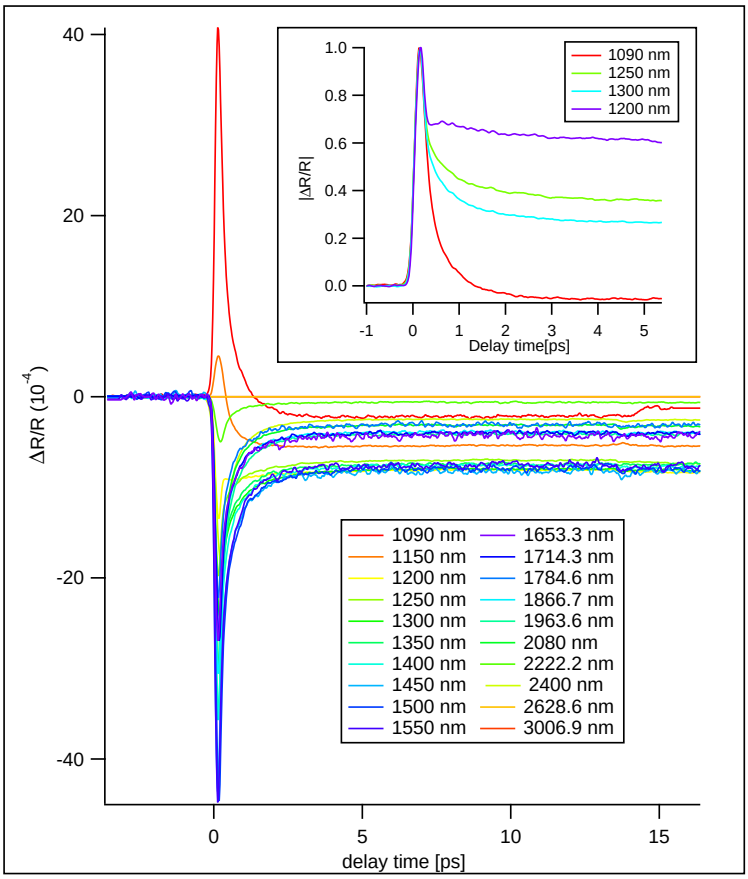


Figure 5.2: Single scan measurement at fixed wavelength and the inset plot is the measurement near the sign change point.

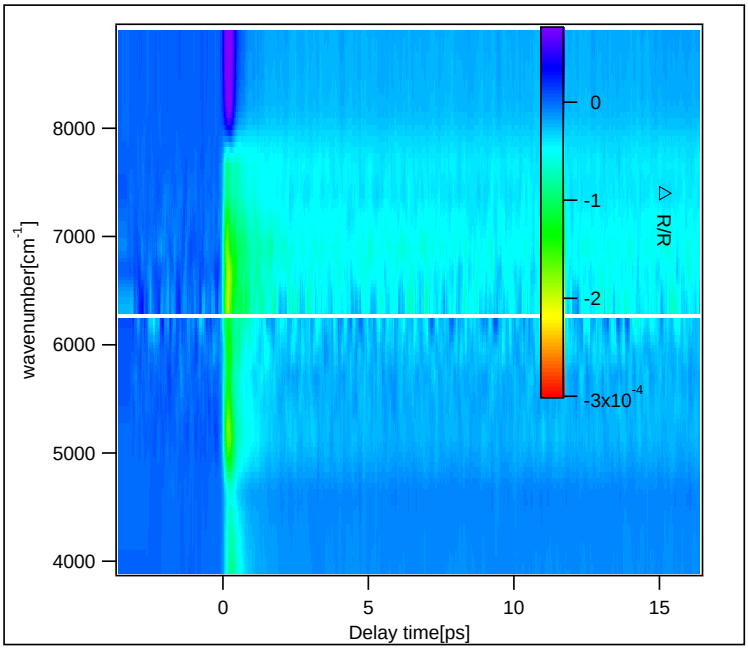


Figure 5.3: The graph is 2D matrix plot at $\phi \sim 44.6\ /cm^2$ in spectral range of 4166.67 - 9174.31 cm^{-1}. A horizontal white line present in the plot is due to the OPA laser source gives too low signal in that spectral range.

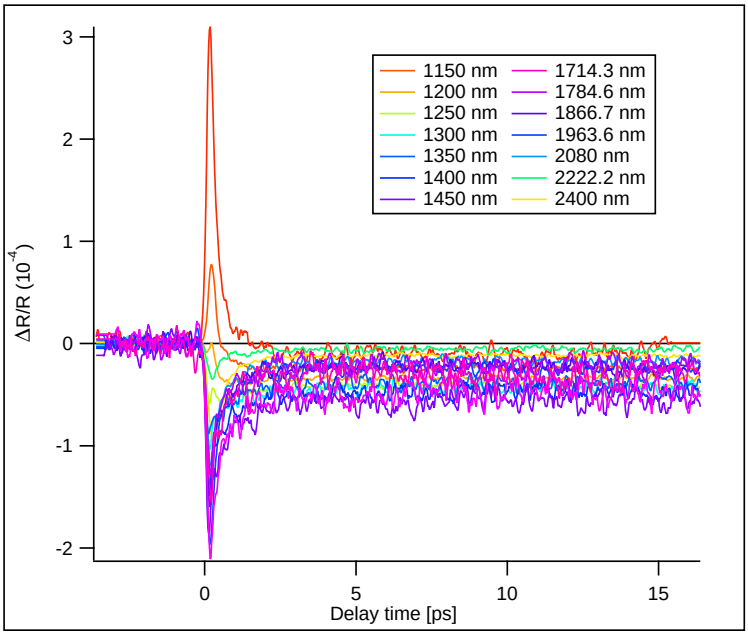


Figure 5.4: Single scan measurement at fixed wavelength

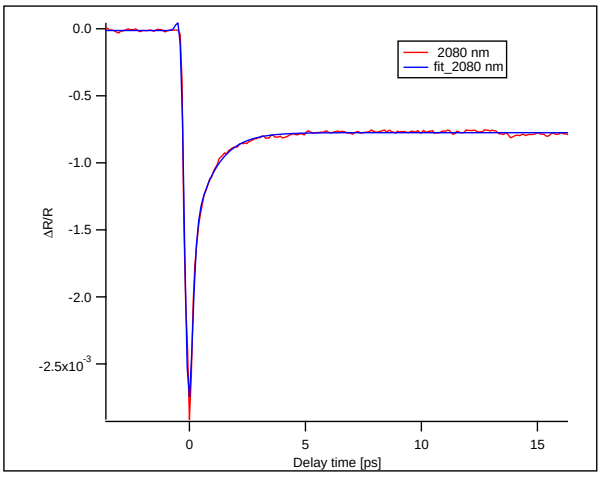


Figure 5.5: The fit of single scan measurement at 2080 nm wavelength.

1046.4 fs for two dynamics contributing to the signal.

We aquire $\Delta R/R$ versus the wavenumber by taking the line profle of the 2D matrix plot of 5.1 at different instant with vertical slices. Figure 5.6 and 5.7 shows the experimental $\Delta R/R$ versus the wavenumber at different instants of the delay time [1]. Those measurements evidence that the sign change point moves towards higher energies with the delay time.

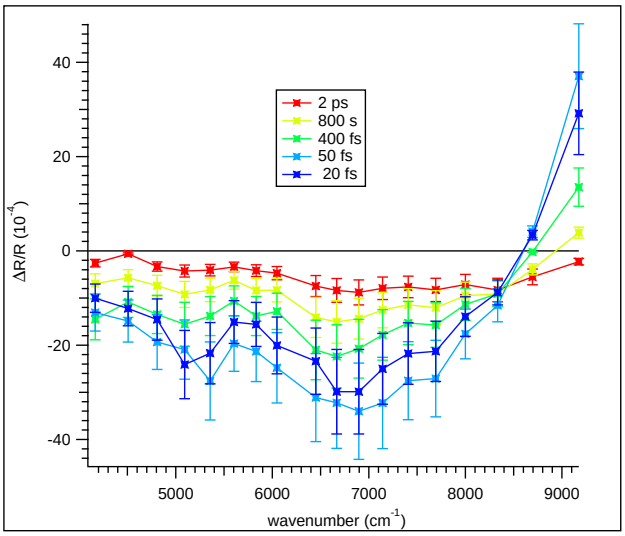


Figure 5.6: The reflectivity variation versus the wavenumber at different delay time in the spectral range of about 4000-9000 cm^{-1} ($\phi \sim 892\ /cm^2$).

[1] Conversion factor:- 1 eV = 8,065.54 cm^{-1} = 1,239.84 nm

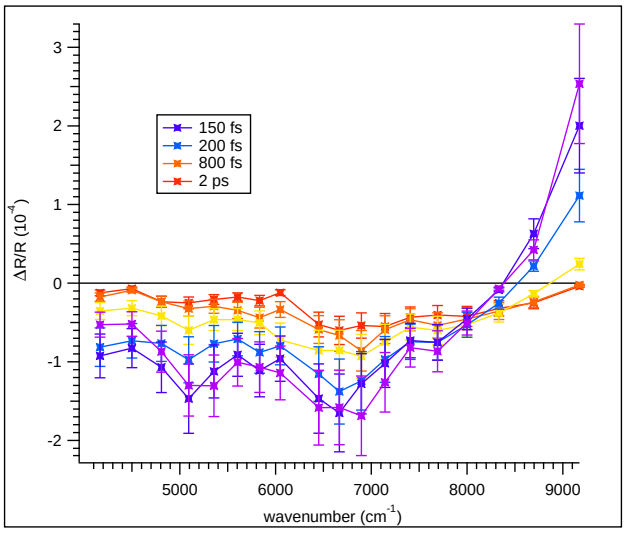


Figure 5.7: The reflectivity variation versus the wavenumber at different delay time in the spectral range of about 4000-9000 cm^{-1} ($\phi \sim 44.6\ /cm^2$).

5.2 Linear Dependence of Differential Reflectivity on absorbed pump fluence

The $\Delta R/R$ measurements at different pump fluences have been conducted in order to check the linearity of $\Delta R/R$ signal and relaxes on the time scale of heat diffusion ($\tau \approx nanoseconds$). Figure 5.8 shows the different $\Delta R/R$ measurements versus delay time. The negative background is due to lattice heating. Figure 5.9 which shows the linear dependence of maximum value of $\Delta R/R$ on absorbed pump fluence.

5.3 Pump-probe experiment with improved spectral resolution

This set of measurement with the monochromator (see experimenatal set-up 4.2) gives detailed spectral information especially near the sign change point. Figure 5.10, 5.11 show the 2D matrix plot and the single scan measurement at a fixed wavelength. In both plots we observe sharp increase of $|\Delta R/R|$ of the signal occurs at zero delay, which corresponds to the incidence pump pulse on the sample. The single scan measurements also shows a fast relaxation dynamics, which was not in measurements

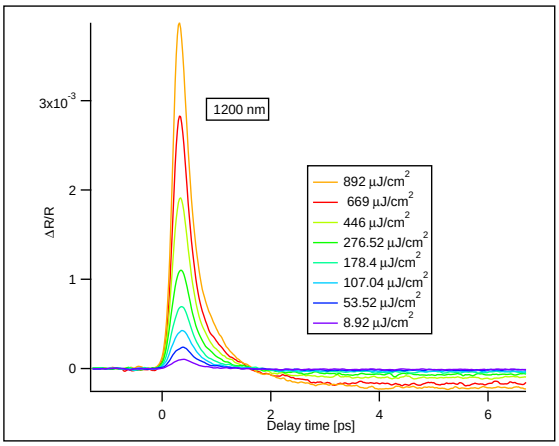


Figure 5.8: Reflectivity variation measurments at different absorbed pump intensities for the in Normal (300K).

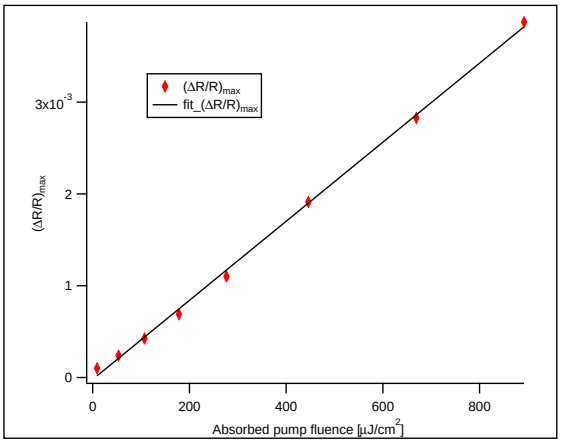


Figure 5.9: Dependence of the absorbed pump intensity versus maximum value of the reflectivity variation

performed with the OPA full-bandwidth (see section 5.1). This fast dynamics could be either an artifact due to wavelengths cross-talking in the monochromator set-up or a physical effect of the improved spectral resolution.

However to avoid this question we mean out about 200 fs to obtain the $\Delta R/R$ trace versus wavelength thus we exploited those measurments mainly to have precise spectral response curves with worse temporal resolution($\approx 200fs$). In figure 5.12 we report the $\Delta R/R$ trace versus wavenumber at zero delay. In this graph a more precise sign change point can be calculated.

5.4 Near-infrared and Supercontinuum Differential Reflectivity

To have a more complete dynamical spectral information we join the set of data obtained in this thesis work in the near infrared spectral range (0.5 - 1 eV) to the data obtained in the visible spectral range (1-2 eV) with the supercontinuum (SC) probe on the same sample by our collaborators [34] and [Giannetti et.al. submitted to Nat. Commun.].

There is a difference in fluence between the two experimental data. In order to

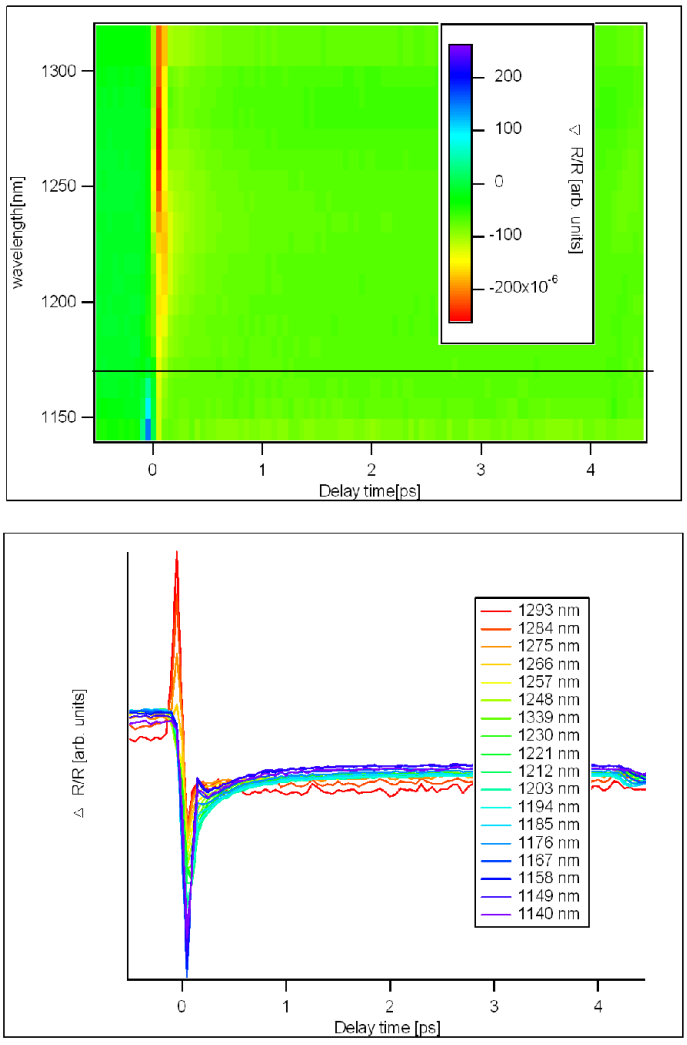


Figure 5.10: The upper graph 2D matrix of single wavelength scans measurments shown in Lower plot in spectral range of 1140 - 1320 nm ($\phi \sim 624.94\ /cm^2$).

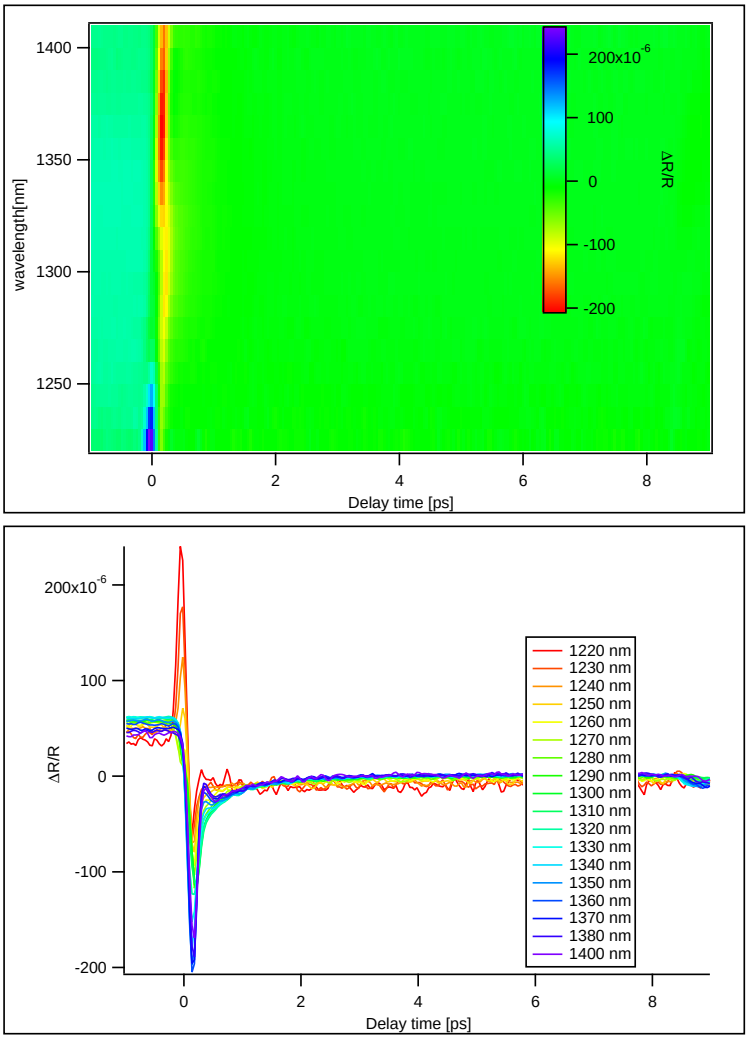


Figure 5.11: The upper graph 2D matrix of single wavelength scans measurments shown in Lower plot in spectral range of 1220 - 1400 nm ($\phi \sim 624.94\ /cm^2$).

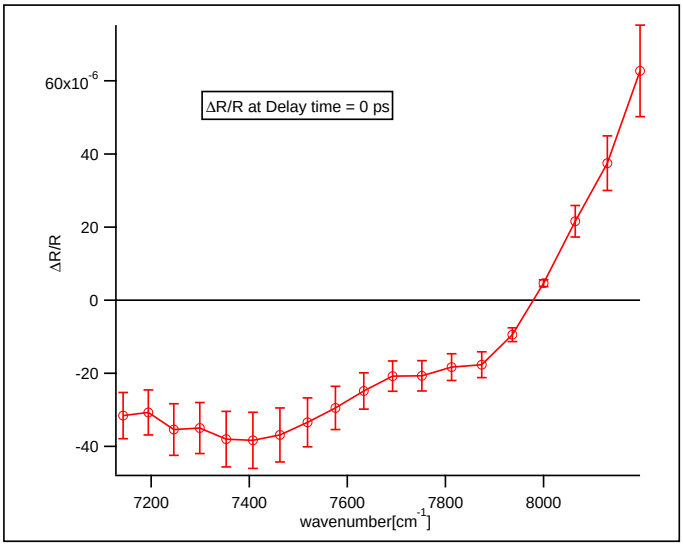


Figure 5.12: The reflectivity variation versus the wavenumber at zero delay time in spectral range of 1140 - 1320 nm ($\phi \sim 624.94\ /cm^2$).

match the data we multiply our measurements by a factor which is equal to the ratio of the fluences. Secondly, to account the difference in the signal due different aquisition methods we did 800 + 800 nm pump-probe measurements. Comparing this data with the supercontinuum probe data at the same wavelength we get a scale factor of 1.4.

The $\Delta R/R$ data of the Supercontinuum part is positive while the IR data is negative at energies below the sign change point ($\approx 8200 cm^{-1}$) while it becomes positive above. Roughly speaking the experimental data resembles the curves proposed in section 3.3.3 from the differential model, when changing ω_p and γ_D of the Drude term. Those aspects will be discussed in more detail in the discussion.

5.5 Sign change dynamics dependence on Fluence

To study the Sign change dynamics related to the ($\Delta R/R = 0$ point) we fitted the $\Delta R/R\,(\omega, t)$ versus the wavenumber (see figure 5.6) with a polynomial of power two at each instant of delay time. We obtain the sign change point by simply finding the zero of the fitted polynomial.

The result is reported in figure 5.14 and it shows the dependence of the sign change

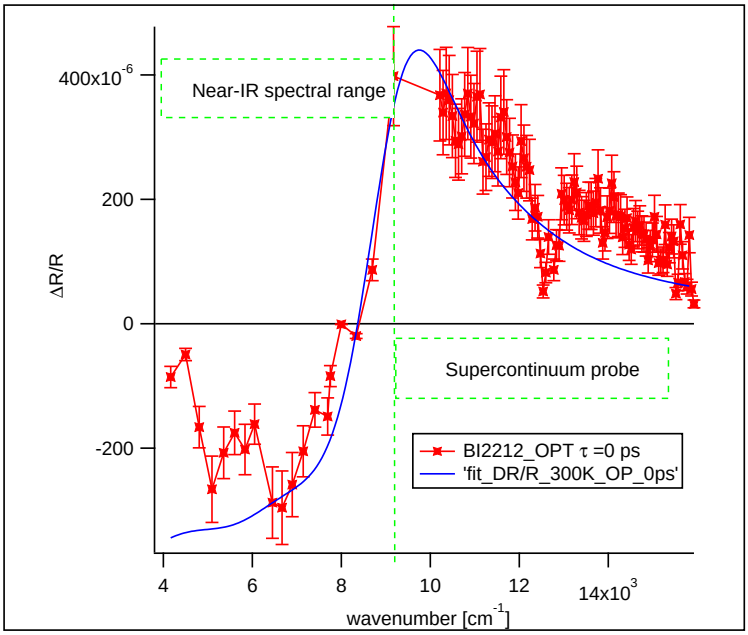


Figure 5.13: The near-infrared and supercontinuum probe fitted with the differentail model.

point ($\Delta R/R = 0$) versus the delay time at different absorbed pump fluences. As the absorbed pump fluence increases the sign change energy ($\Delta R/R = 0$) also increases (see figure 5.15).

The sign change point moves to higher energy as the delay time increase. The sign change dynamics shown in figure 5.16 is fitted with a double exponential function we find $\tau_1 = 960fs$ for the fast peak and $\tau_2 = 1560fs$.

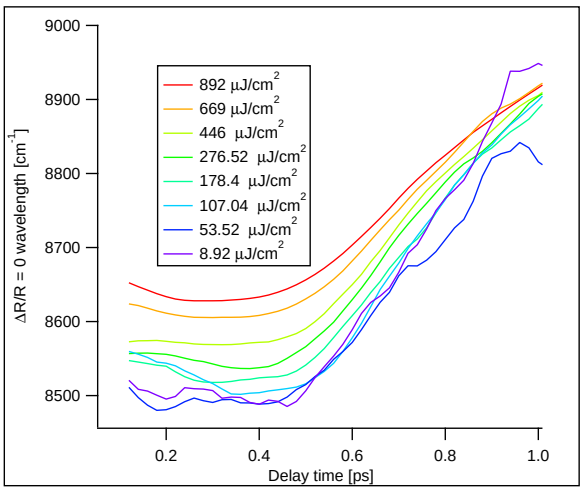


Figure 5.14: $\Delta R/R$ =0 at different absorbed pump fluence in Normal state (300K).

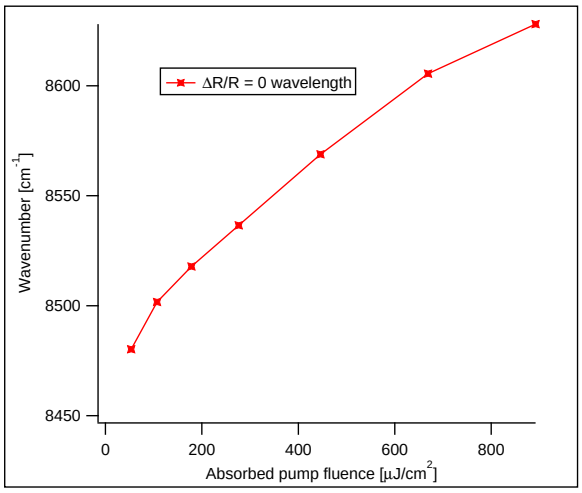


Figure 5.15: Dependence of the absorbed pump intensity versus sign change point of $\Delta R/R$

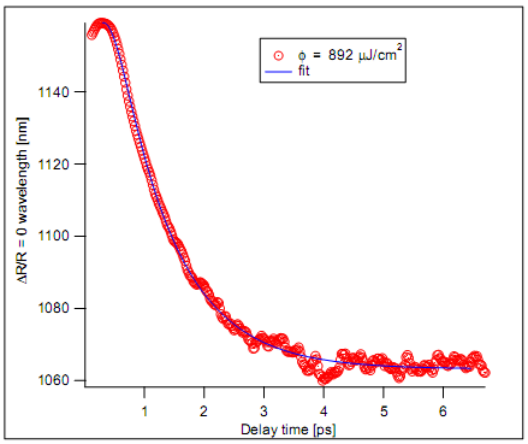


Figure 5.16: Shows the sign change point decay fitted with the double exponential function.

CHAPTER 6

Data Analysis and Discussions of Results

In this chapter we use the theoretical models discussed in section 3.3, to give a description of the non-equilibrium dynamics occuring in the sample during the time-resolved experiments reported in the previous section (see section 5.1).

6.1 Differential Reflectivity Fit

We fit the data $\Delta R/R$ versus the wavenumber by the conventional Drude model. The fit is applied both to the full infrared (IR) spectral range (4166.67 - 9174.31 cm^{-1}) (see figure 6.2) and to the joint IR and SC spectrum (see figure 6.1).

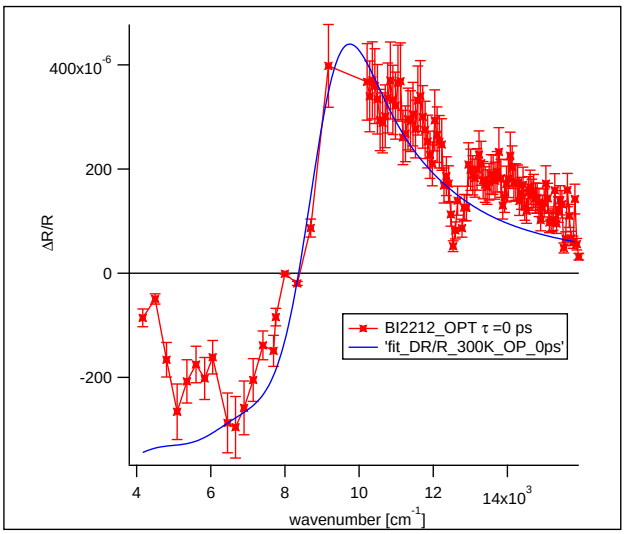


Figure 6.1: Time-resolved reflectivity of both the IR and SC data with the differential fit.

We automatically fit the data in the spectral range of 4166.67 - 9174.31 cm^{-1} with a differential model (see section 3.3.3) and we aquire the new values of γ_D and the ω_P at each instant. The fit is done based on minimizing the χ^2 for the data at each

instant of delay time [35].

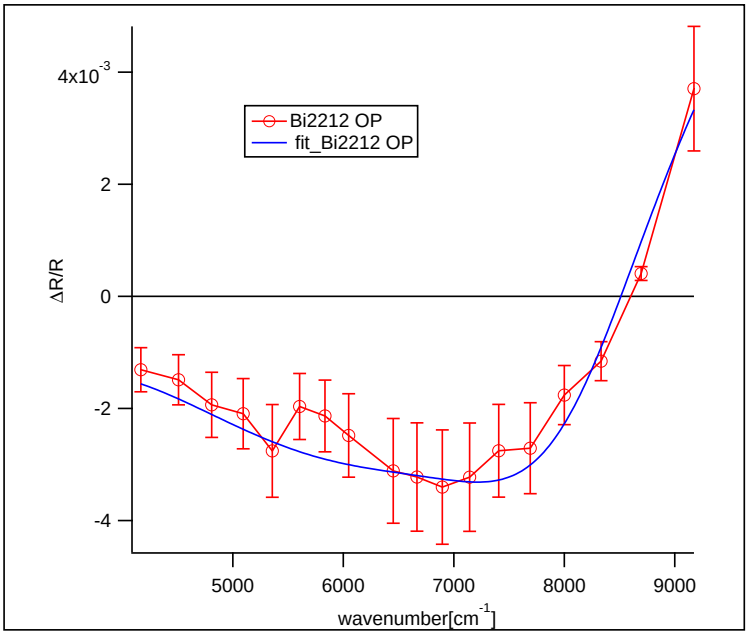


Figure 6.2: Differential reflectivity data and the fit in the 4166.67 - 9174.31 cm^{-1} spectral region.

Here we report the result parameters and the fit in figure 6.3, 6.4. The fit function is given by the following equation.

$$f(t) = \frac{1}{\sigma\sqrt{2\pi}} \int \left(e^{\frac{-\left(t'-t_0\right)^2}{2\sigma^2}} \right) \left(\alpha e^{\frac{-\left(t'-t-t_0\right)}{\tau_1}} + \beta e^{\frac{-\left(t'-t-t_0\right)}{\tau_2}} \right) dt' \qquad (6.1)$$

Where σ is the gaussian duration, α, β are constants, and τ_1, τ_2 are two time recovery dynamics constants. The integral is performed over the time interval of the measurement. The width of the Gaussian function is the temporal Full Width Half Maximum (FWHM) equals the value obtained by the cross-correlation measurement ($\approx$ 80-120 fs) on the pump and the probe.

	τ_1 (in fs)	τ_2(in fs)
γ_D	202	786
ω_p	104	869

Table 6.1: Results of the fit

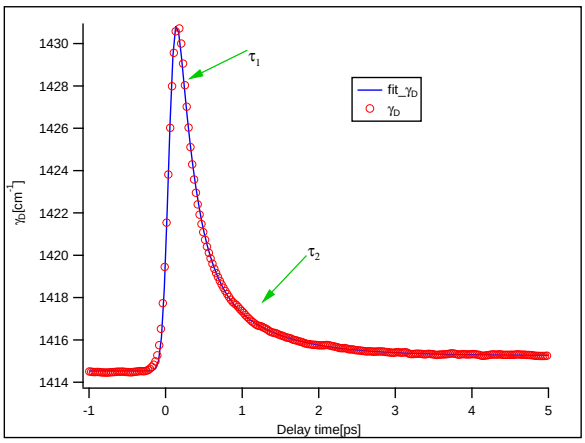


Figure 6.3: The calculated γ_D value (the red circles) and the fit with a three temperature model (in the blue lines).

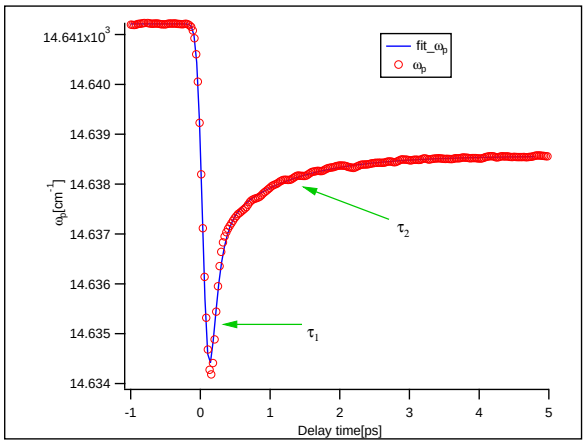


Figure 6.4: The calculated ω_p value (the red circles) and the fit with a three temperature model (in the blue lines).

In table 6.1 we report the fitting results of τ_1 and τ_2 according to the three temprature model the first decay time τ_1 is the relaxation of the hot electron and some strongly coupled bosons while the second decay time τ_2 is the relaxation of hot phonons to the substrate lattice. In the fit we find that τ_1 from ω_p is half of the value calculated from the γ_D. The first few hundred femtoseconds of the dynamics is dominated by electronic response (in the Normal state) to the incident pump pulse [8], [2] so we can write $\omega_p \propto -T_e^2$, where T_e is the electronic temperature in the contrary $\gamma_D \propto T_e$ [14, 13]. And if we assume that $T_e \propto e^{-t/\tau_1}$ it supports pretty well our result.

6.2 Fleunce Dependence of $\Delta\gamma_D$ and $\Delta\omega_p$

We apply the same procedure but for a different fluence. We report figure 6.5, and 6.6 which shows the dependence of $\Delta\gamma_D$ and $\Delta\omega_p$ on the absorbed pump fluence (ϕ).

$$\Delta\gamma_D = \gamma_{D,new} - \gamma_{D,stat} \tag{6.2}$$

Where $\Gamma_{D,new}$ is the new calculated value from the fit and $\Gamma_{D,stat}$ is the calculated during the fit of the equilibrium static reflectivity (see table 3.1). A Similar formula is applied to calculate the $\Delta\omega_p$.

The dependence of the $\Delta\gamma_D$ is linear and increasing while the $\Delta\omega_p$ have a power law dependence($\alpha = 1.2$) on the absorbed fluence.

From the papers published by Basov and Molegraaf we have a linear dependence in temperature for the γ_D and quadratic temperature dependence for the plasma frequency [13, 14]. When the absobed pump fluence increase the temperature of the sample increases (i.e approximately both have linear relationship). Now based on this, comparing with the results that we find for γ_D it gives as a good result so to for ω_p.

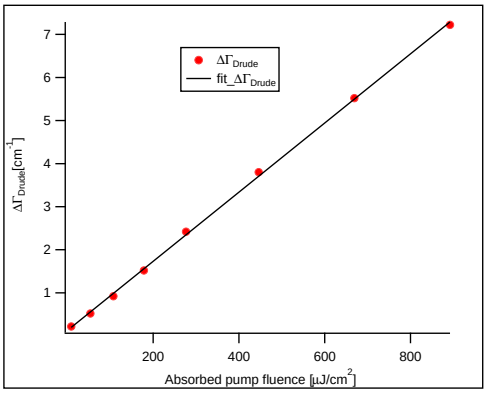


Figure 6.5: Linear dependence on the absorbed pump fluence of the calculated change of Drude gamma at each instant of the delay time.

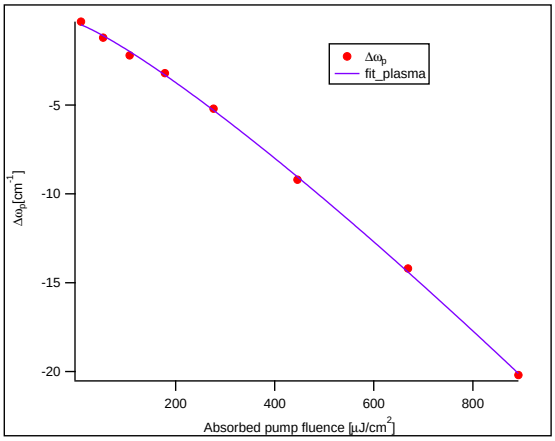


Figure 6.6: Power law dpendence on the absorbed pump fluence of the calculated plasma frequency at each instant of the delay time.

CHAPTER 7

Conclusion

In this thesis work we have reported time-resolved optical spectroscopy data for Bi2212 optimally doped at 300K. A double exponential decay dynamics is ubiquitous in the collected data supporting the picture of three temperature model.

The time-resolved reflectivity data collected are fitted with the differential model here developed and proposed. The model is compatible with the exprimental data. The two free parameters, γ_D and ω_p changes 1414 to 1430 cm^{-1} (175-177 mev) and 14641 to 14634 cm^{-1} (1.817-1.816 eV) respectively during the full recovery dynamics of the system. We found a linear dependence in fluence of the $\Delta\gamma_D$ while the $\Delta\omega_p$ decreases with power law (α =1.2). This tells us the differential reflectivity optical properties could possibly determined only by the charge carriers in the Drude part.

A detailed study of the sign change point dynamics of the differential reflectivity in the normal state, evidences the delicate interplay between the two dynamics of the Drude electrons lifetime and plasma frequency.

The main experimental achievement in this thesis work has been the implementation of a monochromator in the time-resolved set-up to strongly improve the spectral resolution on the sign change of the differential reflectivity.

A further improvement of this work consists in performing a differential reflectivity fit of the $\Delta R/R$ data by using the one-componenet approach (Extended drude model) and can be applied for different samples.

References

[1] Robert J. Cava. Oxide superconductors. *Journal of the American Ceramic Society*, 83(1), 2000.

[2] Roman Sobolewski. Ultrafast dynamics of nonequilibrium quasi-particles in high-temperature superconductors. volume 3481, pages 480–491. SPIE, 1998.

[3] Davide Bossoni. Non-equilibrium infrared optical spectroscopy of high t_C superconductors. Master's thesis, 2010.

[4] J.G. Bednorz and K.A. Mueller. Possible high tc superconductivity in the ba-la-cu-o system. *Z.Phy B*, 2(64):189–193, 1986.

[5] W. N. Hardy, D. A. Bonn, D. C. Morgan, Ruixing Liang, and Kuan Zhang. Precision measurements of the temperature dependence of $\lambda in \mathrm{yba}_2 cu_3 o_{6.95}$: Strong evidence for nodes in the gap function. *Phys. Rev. Lett.*, 70(25):3999–4002, Jun 1993.

[6] K. McElroy, Jinho Lee, J. A. Slezak, D.-H. Lee, H. Eisaki, S. Uchida, and J. C. Davis. Atomic-Scale Sources and Mechanism of Nanoscale Electronic Disorder in Bi2Sr2CaCu2O8+delta. *Science*, 309(5737):1048–1052, 2005.

[7] Damascelli Andrea, Hussain Zahid, and Shen Zhi-Xun. Angle-resolved photoemission studies of the cuprate superconductors. *Rev.Mod.Phys.*, 75(2):473–541, Apr 2003.

[8] L. Perfetti, P. A. Loukakos, M. Lisowski, U. Bovensiepen, H. Eisaki, and M. Wolf. Ultrafast electron relaxation in superconducting $bi_2 sr_2 cacu_2 o_{8+\delta}$ by time-resolved photoelectron spectroscopy. *Phys. Rev. Lett.*, 99(19):197001, Nov 2007.

[9] JR Charles P. Poole. *Handbook of Superconductivity*. Academic press, 2000.

[10] N. F. Mott. *Metal-Insulator Transitions*. Taylor Francis, 1990.

[11] Fredrick Wooten. *Optical properties of solids*. Acadamic press, 1972.

[12] A. Toschi and M. Capone. Optical sum rule anomalies in the cuprates: Interplay between strong correlation and electronic band structure. *Phys. Rev. B*, 77(1):014518, Jan 2008.

[13] D. N. Basov and T. Timusk. Electrodynamics of high-tc superconductors. *Reviews of Modern Physics*, April 2005.

[14] H. J. A. Molegraaf, C. Presura, D. van der Marel, P. H. Kes, and M. Li. Superconductivity-Induced Transfer of In-Plane Spectral Weight in $Bi_2Sr_2CaCu_2O_{8+\delta}$. *Science*, 295(5563):2239–2241, 2002.

[15] Paolo Calvani. Infrared optical properties of high-t_c cuprates. pages 233–268, 1994.

[16] T.Gu G. D Hwang, J.Timusk. High-transition-temperature superconductivity in the absence of the magnetic-resonance mode. *Nature*, 427.

[17] P. B. Allen. Electron-phonon effects in the infrared properties of metals. *Phys. Rev. B*, 3(2):305–320, Jan 1971.

[18] E. van Heumen et. al. Doping-dependent optical properties of bi2201. *New Journal of Physics*, 11(5):055067, 2009.

[19] D N Basov A V Puchkov and T Timusk. The pseudogap state in high-$t_c$superconductors: an infrared study. *Journal of Physics: Condensed Matter*, 8(48), 1996.

[20] S.L.Anisimov et.al. Electron emission from metal surfaces exposed to ultrashort laser pulses. 39:375–377, 1974.

[21] Philip B. Allen. Theory of thermal relaxation of electrons in metals. *Phys. Rev. Lett.*, 59(13):1460–1463, Sep 1987.

[22] P. B. Allen and R. C. Dynes. Transition temperature of strong-coupled superconductors reanalyzed. *Phys. Rev. B*, 12(3):905–922, Aug 1975.

[23] M. L. Schneider et. al. Ultrafast carrier relaxation dynamics in single-layer cuprates. *Europhys. Lett.*, 60(3):460–466, 2002.

[24] R. Rosei, C. H. Culp, and J. H. Weaver. Temperature modulation of the optical transitions involving the fermi surface in ag: Experimental. *Phys. Rev. B*, 10(2):484–489, Jul 1974.

[25] R. W. Boyd. *Nonlinear Optics*. Academic Press, Boston, 2003.

[26] Carlo Antoncini. Ultrashort laser pulses.

[27] Cohrent Inc. Sources. *Expander-Compressor manual*.

[28] Cohrent Inc. Sources. *Mira seed maual*.

[29] Cohrent Inc. Sources. *Optical parametric Amplifier Manual*.

[30] Cohrent Inc. Sources. *RegA Manual*.

[31] Keller et.al. Femtosecond pulses from a continuously self-starting passively mode-locked ti: Sapphire laser. *Optics Letters*, 16(13):1024, 1991.

[32] Ametek Signal Recovery. Technical note tn 1000,technical note tn 1001 and application note an 1003. Technical report.

[33] Damiano Nardi. Time-resolved optical spectroscopyof $cugeo_3$. Master's thesis, 2006.

[34] Fedrico Cilento. Dinamiche elettroniche fotoindotte in superconduttori ad alta temperatura critica. Master's thesis, 2008.

[35] Alexey Kuzmenko. *Guide to RefFIT software to fit Optical spectra*, 2009.